

---

# Towards Increasing Atomic Coherence Times with a Standing Wave Dipole Trap

Derya Taray

---



Munich 2020



---

# Zur Verbesserung atomarer Kohärenzzeiten durch eine Stehwellen-Dipolfalle

Derya Taray

---

Masterarbeit  
an der Fakultät für Physik  
der Ludwig-Maximilians-Universität  
München

vorgelegt von  
Derya Taray  
aus Hannover

München, den 13.05.2020

Gutachter: Prof. Dr. Harald Weinfurter  
Betreuer: Tim van Leent

*"It's a trap!"*  
- Admiral Gial Ackbar,  
Battle of Endor



# Contents

<b>1. Introduction</b>	<b>1</b>
<b>2. Experimental Setup</b>	<b>3</b>
2.1. Atomic Quantum Memory	3
2.2. Trapping the Atom	3
2.2.1. Magneto Optical Trap	4
2.2.2. Dipole Trap	5
2.3. Control of magnetic fields	7
2.4. Entanglement Generation	8
2.4.1. Atom-Photon Entanglement	8
2.4.2. Atom-Atom Entanglement	9
2.5. Atomic State Readout	10
2.6. Towards Longer Distances	11
2.6.1. Coherence Requirements	12
2.6.2. Photon collection losses	13
<b>3. Decoherence Mechanisms</b>	<b>15</b>
3.1. State evolution of a spin 1 system	15
3.1.1. Magnetic field in x-direction	16
3.1.2. Magnetic field in y-direction	17
3.1.3. Magnetic field in z-direction	17
3.1.4. Circular Dipole Trap Polarization	18
3.2. Polarization Effects of a Strongly Focussed ODT	19
3.3. Evolution of the Atomic State in the Effective ODT field	22
3.3.1. Simulation	22
3.3.2. Parameter configuration for the Bell Test	23
3.4. Increasing the coherence Time	24
3.4.1. Magnetic Guiding Field	25
3.4.2. Lower Atomic Temperature and Potential Depth	26
3.4.3. State Transfer	27
3.4.4. Summary	28
<b>4. Standing Wave Dipole Trap</b>	<b>31</b>
4.1. Geometry of a Standing Wave Dipole Trap	31
4.2. Elimination of Circular Polarisation	34
4.3. The Effect of Misalignments	34
4.3.1. Transversal Displacement	35

## Contents

4.3.2. Longitudinal Displacement . . . . .	36
4.3.3. Angular Misalignment . . . . .	37
4.3.4. Different Focus Waists . . . . .	40
4.3.5. Different Intensities of the Beams . . . . .	41
4.3.6. Summary . . . . .	42
4.4. Loading the Atom in the Central Pockets . . . . .	46
4.4.1. Detecting the Position of the Atom . . . . .	47
4.4.2. Moving the Atom to the Centre . . . . .	48
4.5. Trap Operation . . . . .	50
<b>5. Experimental tests</b>	<b>51</b>
5.1. Spatial Overlap . . . . .	51
5.1.1. Setup . . . . .	52
5.1.2. Measurement Procedure . . . . .	55
5.1.3. Evaluation of the Results . . . . .	56
5.1.4. Discussion . . . . .	58
5.2. Phase Stability . . . . .	61
5.2.1. Setup . . . . .	62
5.2.2. Analysis of the Setup . . . . .	63
5.2.3. Measurements . . . . .	64
5.2.4. Summary . . . . .	66
<b>6. Summary and Outlook</b>	<b>67</b>
<b>A. Coordinate System and Polarizations</b>	<b>69</b>
<b>B. Quantification of the Circularity of Light</b>	<b>71</b>
<b>C. List of Abbreviations</b>	<b>75</b>
<b>D. Tables</b>	<b>77</b>
D.1. Physical Constants . . . . .	77
D.2. Physical Properties of $^{87}\text{Rb}$ . . . . .	77
D.3. Fit Parameters from the Knife Edge Measurements . . . . .	78

# 1. Introduction

The development of quantum mechanics in the first half of the last century, raised vast discussions whether indeed a nonlocal or non deterministic theory could be the fundamental description of nature. On the one hand, quantum mechanics has proven to be an extremely powerful tool to describe experimental results. On the other hand, entanglement of remote particles, which is intrinsically contained in quantum mechanics, violates basic assumptions one would expect a complete theory of the world to fulfil from the experiences of daily life. These assumptions are often referred to as locality, and reality. Locality assumes that there can not be a causal connection between space-like separated events and is a very fundamental assumption of many well-established theories like general relativity. Reality, states that all quantities that can be predicted with certainty from the theory, have a counterpart in the real world. Combined with the requirement of completeness, it states, that all properties in the real world, exist independently from observation or interaction with other parts of reality.

One of the most important formulations of the contradiction between quantum mechanics and intuitive expectations on a model of our physical reality, was formulated in the famous Einstein-Podolski-Rosen (EPR) paradox [13]. The conclusion of this trio was that the quantum mechanical description of the world cannot be complete in the sense, that an underlying theory can be found, that will restore locality and reality. Such theories are nowadays called local hidden variable (HV) theories.

Decades later, John Bell derived under the assumptions of locality and reality an inequality, that gave an upper bound to certain correlation measurements in any local realistic HV theory [5]. In a reformulation [10], this inequality provided an experimental test, whether the world the experiment is done in, can be described completely by a local realistic theory. These experiments require the preparation of an entangled state of two distant systems and simultaneous measurements of two non commuting observables of these.

Additional difficulties for these Bell tests, arise from the necessity of the different measurements to be space like separated and achieve a detection efficiency above  $\frac{2}{3}$ . If these requirements are not fulfilled, so called loopholes for local HV theories remain. In the last years several "loophole-free" violations of Bell's inequality were realised [15, 18, 33], proving the inability of local realistic theories to describe the real world completely.

The philosophical implications of these results remain open for discussion however, nowadays the peculiar properties of entangled systems are rather regarded as a possibility for technological development instead of a fundamental problem of the scientific world view. Quantum algorithms promise an exponential speed-up in certain computational problems and quantum cryptography offers inherently secure communication protocols [6, 21].

## 1. Introduction

To enable distributed quantum computing and for many quantum cryptography protocols, sharing an entangled state between distant nodes is required. This can be achieved by a quantum network, consisting of nodes that can be entangled with each other via quantum links [21]. Quantum repeater methods can be used to entangle nodes, that are not directly connected [8]. In order to connect different cities in such a network with a feasible number of nodes, link lengths up to 100 km are desired. Additionally, longer distances between entangled nodes, will allow to shrink the parameter-space for local realistic theories by Bell tests with increased space-like separation.

One limitation on the achievable length of the quantum link, are growing times for classical communication between the nodes, that require longer coherence of the combined node state. Also to share a state between two not directly connected nodes, both have to remain coherent, until the link is established. For these two reasons, the coherence time of the used quantum memory is a crucial quantity of any quantum network link.

This work was conducted at an experiment, implementing a quantum network link over a distance of 398 m with a system of two entangled atoms, trapped in tightly focussed optical dipole traps. The distance between the two nodes is planned to be increased to 20 km in the near future. In order to achieve this goal, a longer coherence time of the atomic qubit is required. Currently it is limited by longitudinal field components originating from a strongly focussed optical dipole trap. This effect can be cancelled by using a standing-wave trap configuration, promising an increase in coherence time by up to two orders of magnitude.

Chapter 2 will explain details of the experiment. Chapter 3 will introduce the main decoherence mechanism and approaches to reduce it at the cost of repetition rate. Chapter 4 will explain the possibility to cancel the effect entirely with a standing wave dipole trap, consisting of two counter-propagating beams. Criteria for the alignment and phase stabilisation of the two beams will be derived. Chapter 5 will present two setups, that were built in the scope of this work, to test the achievable precision of the alignment by fibre coupling and stabilisation of the relative phase between the beams with two acousto-optic modulators.

## 2. Experimental Setup

To realize a quantum network link, entanglement needs to be shared between two distant nodes. In the experiment described here, these nodes consist of two single  $^{87}\text{Rb}$  atoms, separated by 400 m. The experiment was built over the past 20 years, leading to successful atom-photon entanglement [39] and finally a loophole free violation of Bell's inequality [33] [9]. To achieve this, a high fidelity of the entangled state and a fast readout of the quantum memories was required. During the Bell test, the fidelity was 83% and the state readout was done within 800ns.

In this chapter the basics of this experiment will be summarized together with current limitations of the system. Sections 2.1 and 2.2 will explain the atomic system used as well as the trapping setup. Section 2.3 will shortly explain the control of magnetic fields in the setup. Section 2.4 will describe how the entanglement between the nodes is generated. Section 2.5 explains the readout of the quantum memory and section 2.6 will summarize the requirements arising when increasing the distance between the nodes, and current limitations of the setup.

### 2.1. Atomic Quantum Memory

The quantum node consists of a single  $^{87}\text{Rb}$ -atom, chosen because of its well known, hydrogen-like level structure. The nuclear spin of  $^{87}\text{Rb}$  is  $I = \frac{3}{2}$ , therefore its ground state  $5S_{1/2}$  is split into the hyperfine levels  $F=1$  and  $F=2$  [36]. The  $5P_{1/2}$  and  $5P_{3/2}$  split up into  $F'=1,2$  and  $F'=0,1,2,3$  respectively.

The atomic qubit is encoded in the Zeeman states  $F=1$ ,  $m_F=\pm 1 = |1, \pm 1\rangle$  of the ground state, noted  $|\uparrow\rangle_z / |\downarrow\rangle_z$  respectively, according to the convention for a two state system for the eigenstates of the  $\sigma_z$  Pauli-matrix. As the degeneracy of the Zeeman states can be lifted by optical and magnetic fields, precise control of these is essential to achieve a high quality quantum memory. The eigenstates of the Pauli  $\sigma_{x/y}$  operators are noted  $|\uparrow\rangle_{x/y} / |\downarrow\rangle_{x/y}$  (also see Table A.1).

For a level scheme see figure 2.1.

### 2.2. Trapping the Atom

In order to efficiently control the state of the atom, drive transitions and collect scattered light, its spatial position has to be controlled precisely. In the described experiment, this is achieved by holding a cloud of cooled atoms in a magneto-optical trap (MOT) inside a ultra high vacuum (UHV) glass cell, allowing optical access from many directions. A

## 2. Experimental Setup

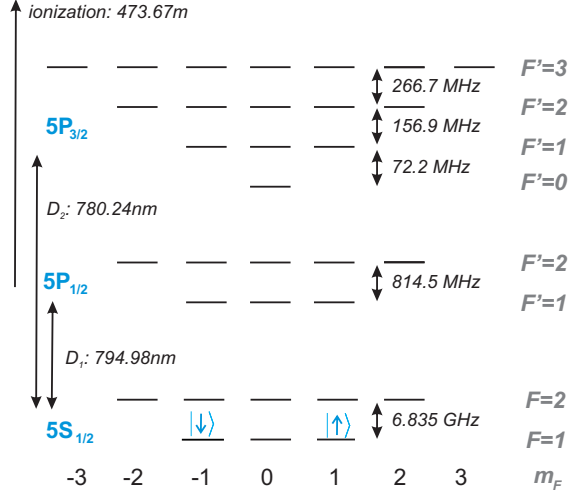


Figure 2.1.: Scheme of relevant levels in  $^{87}\text{Rb}$

strongly focussed optical dipole trap (ODT) picks out one atom, that is consequently used in the experiments.

### 2.2.1. Magneto Optical Trap

In order to load an atom in the shallow potential of the ODT, which is only several mK deep, it has to be cooled to roughly that temperature range first. This is done in a MOT, using three perpendicular pairs of counterpropagating, circularly polarized cooling lasers, which are 18MHz red detuned to the  $5S_{1/2}$   $F=2 \rightarrow 5P_{3/2}$   $F'=3$  transition. In this configuration an atom will preferably absorb light from a beam that is propagating against the direction it moves in, and therefore get decelerated by the momentum exchange with the photons. This process is called Doppler-cooling, and one can reach temperatures down to  $146\mu\text{K}$  for  $^{87}\text{Rb}$  [36]. In this specific configuration also polarization gradient cooling occurs, resulting in even lower temperatures [12].

The cooling transition is closed, however there is a finite probability for an atom to be excited off-resonantly to the  $5P_{3/2}$   $F'=2$  state, and then decay to the ground level. In order to still cool efficiently, all cooling lasers are thus overlapped with additional repump lasers, resonant to the  $5S_{1/2}$   $F=1 \rightarrow 5P_{3/2}$   $F'=2$  transition, from where they can decay spontaneously back into the lower state of the cooling transition.

Additional to the cooling, the atom cloud has to be confined in a potential. In the MOT, this is achieved by a magnetic quadrupole field with a minimum at the centre. As the cooling lasers are red detuned to the cooling transition, the Zeeman-shift due to the magnetic field will bring the transition frequency closer to the cooling laser's frequency. As the magnetic field is increasing towards the outside of the trap, this will result in a position-dependent scattering rate. This increase in scattering rate outside the centre, resulting in more momentum transfer, will produce an effective potential for

the atoms, with a minimum at the centre of the MOT, where the magnetic field is zero. The transition will get more resonant to the cooling lasers, because of their circular polarization, that only addresses the  $m_F$  states, that approach each other in a magnetic field.

### 2.2.2. Dipole Trap

Next, a single atom from the cooled and confined cloud is loaded into the optical dipole trap. It consists of a laser beam with a wavelength  $\lambda = 852nm$ , detuned to both the  $D_1$  and  $D_2$  line, focused by a high NA objective to  $1.92\mu m$  waist. The far red detuned ODT light will create an AC-Stark shift of the ground state, introducing an intensity dependent potential for the atom[22]. Thus the atom can be stored in the centre of the focus. The energy shift of the  $m_F = 0/\pm 1$  ground states can be calculated as:

$$\Delta E(\vec{r}) = -\frac{\pi c^2 \Gamma}{2\omega_0^3} \left( \frac{1 - P g_F m_F}{\delta_{1,F}} + \frac{2 + P g_F m_F}{\delta_{2,F}} \right) \cdot I(\vec{r}), \quad (2.1)$$

where  $\Gamma$  is the decay rate and  $\omega_0$  the frequency of the atomic transition,  $g_F$  the Landé factor,  $\delta_{1,F}$  and  $\delta_{2,F}$  the detunings to the  $D_1$  and  $D_2$  line,  $I(\vec{r})$  the light field intensity and  $P$  quantifies the circularity of the light's polarization with  $P = \pm 1$  for  $\sigma^\pm$  light, and  $P=0$  for linear polarization. For the exact definition see App. B. Note the qubit-states are shifted differently in a circular polarized light field. This effect will be discussed in more detail in Section 3.1.4. For this reason the ODT lights polarization is set to linear by a polariser, see App. A for a definition of polarisations and coordinate system.

#### Trap Geometry

From Equation 2.1 it is obvious that the potential is proportional to the intensity of the ODT light field, which can be approximated by a Gaussian beam  $I(\vec{r}) = \frac{1}{2}c\epsilon_0 \left| \vec{\mathcal{E}}(\vec{r}) \right|^2$  with the electric field of a linearly polarized beam in  $TEM_{00}$  mode [41]:

$$\vec{\mathcal{E}}(\vec{r}) = \mathcal{E}_0 \cdot \hat{e}_x \frac{w_0}{w(z)} \exp \left( -\frac{x^2 + y^2}{w(z)^2} + i\varphi_{00}(\vec{r}) \right), \quad (2.2)$$

with the maximum value of the electric field:  $\mathcal{E}_0$ , the unity vector in x direction  $\hat{e}_x$ , and the minimum waist of the beam  $w_0 = 1.92 \mu m$  for this experiment. The coordinate system is such, that the beam propagates in z-direction and x is the horizontal direction in the laboratory (see App A). The beam waist, dependent on the position along the

## 2. Experimental Setup

optical axis  $z$ , is given by:

$$w(z) = w_0 \sqrt{1 + \left(\frac{z}{z_R}\right)^2}, \quad (2.3)$$

it is the radius around the beam axis, within which  $1 - e^{-2}$  of the total power is transmitted.  $z_R = \frac{\pi w_0^2}{\lambda} = 13.6 \mu\text{m}$  is the Rayleigh length, i.e. the distance from the focus, where  $w(z) = \sqrt{2} w_0$ .

The phase of the Gaussian beam in  $TEM_{00}$  mode consists of several terms:

$$\varphi_{00}(\vec{r}) = \omega t + kz + k \frac{x^2 + y^2}{2R} - \arctan\left(\frac{z}{z_R}\right) \quad (2.4)$$

The first two terms  $\omega t + kz$  with  $k = \frac{2\pi}{\lambda}$ , are the normal phase evolution of a plane wave. Note that this beam is propagating along the  $z$ -axis in negative direction. The third term:  $k \frac{x^2 + y^2}{2R}$  with  $R = z(1 + \frac{z^2}{z_R^2})$ , introduces the curvature of the wavefront. The last term,  $\arctan\left(\frac{z}{z_R}\right)$  is the Gouy-phase, that introduces a phase shift of  $\pi$  between the far fields on both sides of the focus; this becomes larger in higher order transversal modes.

Calculating the intensity, and collecting all constant factors into the maximum trap depth  $U_0$  one can write the potential, the atom experiences as:

$$U(\vec{r}) = -U_0 \frac{1}{1 + \frac{z^2}{z_R^2}} \exp\left(-\frac{2(x^2 + y^2)}{w(z)^2}\right) \quad (2.5)$$

In order to derive longitudinal and transversal oscillation frequencies of the atom's movement in the trap, this potential can be approximated by a three dimensional harmonic oscillator potential. The spring constants  $k_x = k_y = \frac{4U_0}{w(z)^2}$ , and  $k_z = \frac{2U_0}{z_R^2}$  are calculated by approximating the  $x, y$  and  $z$  dependent part of the potential to second order. This is valid for atomic temperatures well below the trap depth. By changing the power of the laser,  $U_0$  can be varied between  $k_B \cdot 0.3 \text{mK}$  and  $k_B \cdot 3.2 \text{mK}$ , corresponding to maximally 60mW, what is easily possible with commercial laser diodes. From this, the longitudinal ( $z$ ) and transversal ( $x/y$ ) trap frequencies can be calculated to lie in the range:

$$\begin{aligned} \omega_T &= \sqrt{\frac{k_x}{m}} = 2\pi \cdot 36 \dots 118 \text{ kHz} \\ \omega_L &= \sqrt{\frac{k_z}{m}} = 2\pi \cdot 3.6 \dots 11.8 \text{ kHz} \end{aligned} \quad (2.6)$$

Mind that the Gaussian-shaped potential was approximated by a harmonic oscillator, with the same oscillation frequency, for all energy levels. In the real potential, different atoms, will have slightly different oscillation frequencies. Also  $\omega_T$  still has a dependency on the z-position, as it is inverse proportional to the local waist  $w(z)$ , but this effect will be minimal within the values of  $z$ , the atom can reach.

#### Trap Operation

The ODT is loaded by overlapping the centre of the MOT with the ODT focus. By keeping the cooling lasers on, while the atoms move through the conservative potential of the ODT, an atom can be trapped in the minimum of the potential. If the ODT is tightly focused, the allowed volume for the atom becomes very small. In this case, the collisional blockade effect limits the maximum number of atoms in the trap to a single one [34].

Since the atom is located in the focus of the objective, the objective can also be used to efficiently collect fluorescence light emitted by the atom. This is used to detect successful loading of an atom in the ODT. Cooling light, scattered by the atom, is collected by the high-NA Objective, coupled out of the ODT-Beam with a dichroic mirror and transferred to an avalanche photo diode (APD) by a single mode fibre. The count rate of this APD increases significantly when an atom is loaded. Figure 2.2 shows a sketch of the described setup.

Once an atom is loaded in the dipole trap, it is transferred in the  $5S_{1/2}F = 1, m_F = 0$  state by optical pumping with two lasers and the experimental sequence is started [9]. During this, several laser pulses are applied to the atom. Since this can lead to heating and loss of the atom the cooling lasers are turned on again at certain points of time. When this is the case, also the fluorescence is checked again and if it has dropped, the setup automatically stops the sequence and loads a new atom before continuing. Of course the probability to loose the atom is higher, if the ODT potential is lower. More details on the experimental sequence can be found in Section 3.3.2.

### 2.3. Control of magnetic fields

Magnetic fields can lift the degeneracy of the  $m_F$  states, in which the atomic qubit is encoded, and therefore create a time evolution of the state. If the magnetic fields fluctuate uncontrolled, this can lead to decoherence. In and around the laboratory, there are several sources of constant and fluctuating magnetic fields, like the field of the earth, public transportation lines and power supplies of lab-equipment. To compensate for these, three pairs of coils are centred around the glass cell and a 3D magnetic field sensor is placed 2 cm away from the position of the atom. These coils can generate a magnetic field of up to  $\pm 500\text{mG}$  in any direction. They are controlled by an active stabilization, that uses the signal from the magnetic field sensor to keep the field close to the atom at a constant value. This feedback loop has a bandwidth of up to 200Hz, allowing to reduce the magnetic field fluctuations to  $0.5\text{mG(rms)}$  [9, 23, 25].

## 2. Experimental Setup

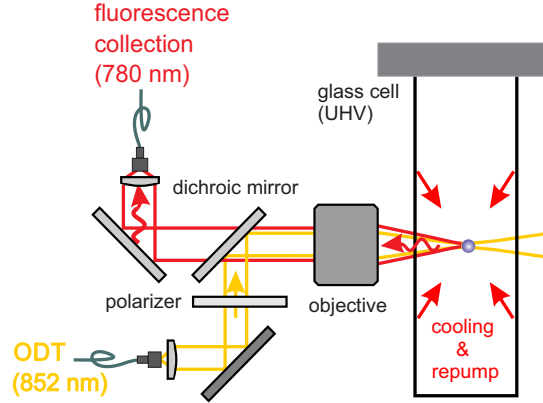


Figure 2.2.: Setup to focus the ODT and collect the fluorescence light

## 2.4. Entanglement Generation

The aim of this experiment is to create entanglement between two distant atoms. Usually some kind of interaction is necessary for the generation of entanglement. But since atoms in optical traps are rather immobile systems it is more feasible, to first generate entanglement between the atoms and a more mobile system like a photon. In this experiment, this atom-photon entanglement is achieved via a spontaneous decay. Then the two photons are brought together and the entanglement is transferred to an atom-atom entanglement via the entanglement swapping protocol. This process will be explained in the next two sections.

### 2.4.1. Atom-Photon Entanglement

Entanglement is generated between the atomic Zeeman state and the polarization of a photon. For this purpose, the atom is prepared in the  $F=1, m_F=0$  ground state.

First the atom is excited to the  $5P_{3/2}, F=0$  state, which spontaneously decays back into one of the ground states  $5S_{1/2}, F=1, m_F=0/\pm 1$  with a lifetime of 26.2ns. To preserve angular momentum, the polarization of the emitted photon, has to be  $\sigma^\pm$  if the atom ends up in the  $m_F = \mp 1$  state and  $\pi$  in case of  $m_F=0$ , see Chapter A for definitions of the polarizations. After this process the atomic state and the polarization of the photon are entangled [39]. Due to different radiation characteristics of the  $\pi$  photons, only the  $\sigma^\pm$  photons are collected by the high-NA objective and coupled into a single mode fibre. The fibre used here, is the same as the one used for the atomic fluorescence detection, therefore an efficient collection of the fluorescence light, indicates also efficient collection of the entangled photon. Figure 2.3 illustrates the described process. Since the Clebsch-Gordan-coefficients of the decay channels are equal, the resulting two particle state provided a photon collection can be written as [39]:

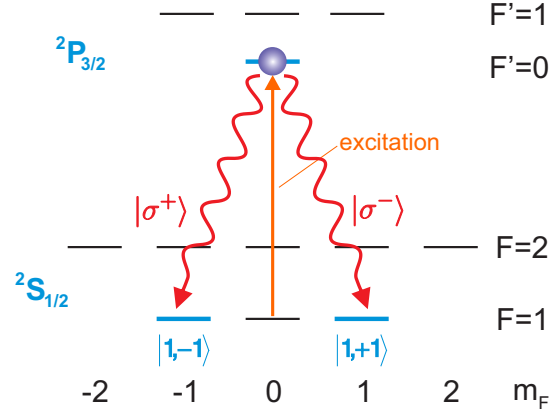


Figure 2.3.: Generation of atom-photon entanglement via spontaneous decay through different channels.

$$|\psi\rangle_{atom,photon} = \frac{1}{\sqrt{2}} (|\uparrow\rangle_z |\sigma^-\rangle + |\downarrow\rangle_z |\sigma^+\rangle) \quad (2.7)$$

This can be expressed in different bases of the polarization:

$$\begin{aligned} |\psi\rangle_{atom,photon} &= \frac{1}{\sqrt{2}} (|\uparrow\rangle_x |V\rangle + |\downarrow\rangle_x |H\rangle) \\ &= \frac{1}{\sqrt{2}} (|\uparrow\rangle_y |M\rangle + |\downarrow\rangle_y |P\rangle) \end{aligned} \quad (2.8)$$

From this, it is obvious, that by measuring the photon polarization in different bases, one can prepare the atom in different states.

### 2.4.2. Atom-Atom Entanglement

In order to entangle two atoms at a distance, atom-photon entanglement is generated in two distant atom traps simultaneously. Both photons are brought together and measured in the maximally entangled Bell-basis [26]. The interferometric Bell State Measurement (BSM) can distinguish between the two different Bell states:

$$|\Psi^\pm\rangle_{photon,photon} = \frac{1}{\sqrt{2}} (|HV\rangle \pm |VH\rangle) \quad (2.9)$$

## 2. Experimental Setup

and gives a signal in case of successful detection [19]. The other two Bell states:

$$|\Phi^\pm\rangle_{\text{photon,photon}} = \frac{1}{\sqrt{2}}(|HH\rangle \pm |VV\rangle) \quad (2.10)$$

cannot be distinguished and are therefore ignored if measured. The BSM setup is shown in figure 2.4.

This is an implementation of the entanglement swapping protocol, leaving the two atoms in one of the following two entangled states [20] [30]:

$$|\Psi^\pm\rangle_{\text{atom,atom}} = \frac{1}{\sqrt{2}}(|\uparrow\downarrow\rangle_x \pm |\downarrow\uparrow\rangle_x) \quad (2.11)$$

Note that the BSM gives a heralding signal when the entangled state has been prepared.

In order to project the photons on an entangled state, a good spatial and temporal overlap at the input of the BSM is essential. The spatial overlap is ensured, by the usage of a fibre beam splitter (BS). For the temporal overlap, the photons have to arrive at the BSM setup at exactly the same time. As this setup is located in the same lab, as one of the traps (trap 1), the photon from the other trap (trap 2), will arrive with a delay of  $3.6 \mu\text{s}$  due to the 700 m fibre, connecting the two labs. In order to still achieve a good temporal overlap of the photons, the excitation in trap 1 is done  $3.6 \mu\text{s}$  later than in trap 2.

## 2.5. Atomic State Readout

After preparing the desired atomic state it can be observed, i.e. it is read out, via a state selective ionization process. By applying a  $\sigma^+$  polarized light pulse, resonant to the  $5S_{1/2}, F = 1 \rightarrow 5P_{1/2}, F' = 1$  transition, the  $m_F = -1, 0$  states can be transferred, while the  $m_F = +1$  state is not, due to conservation of angular momentum. A second beam ionizes the atoms in the  $5P_{1/2}, F' = 1$  level. See figure 2.5 for an illustration. After applying the ionization pulse, the ion and electron are detected with channel electron multipliers [17] [29] or the fluorescence light of the cooling beams is collected again to check whether the atom is still in the trap or has been ionized. This procedure reaches a maximum detection efficiency of 96% corresponding to the probability of the dark state to not be ionized.

In the case of  $\sigma^+$  polarization of the readout pulse,  $m_F = -1, 0$  are called bright state, while the  $m_F = +1$  is a dark state. For different polarizations  $\chi_{ro}$ , the bright and dark states are different superpositions of the  $m_F$  states, such that the measurement basis can be chosen by the polarization of the readout beam. To test whether the atom is in a certain state,  $\chi_{ro}$  is set such, that the state is the dark state and a Pi-pulse is applied.

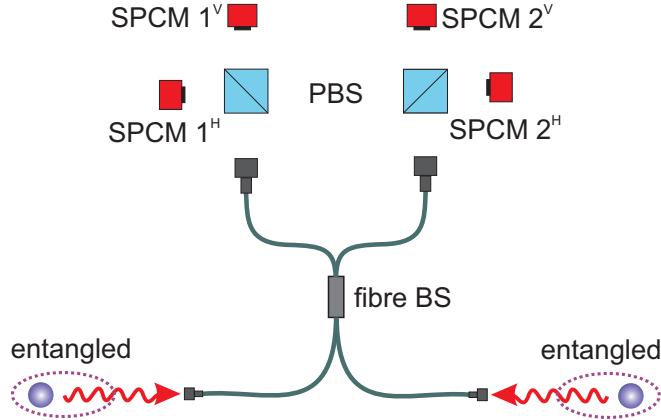


Figure 2.4.: Setup of the BSM: single photon counting modules (SPCMs) are connected to an FPGA, counting coincidences of photon detections. Simultaneous events in  $1^H$  and  $2^V$  or in  $1^V$  and  $2^H$  indicate a projection of the photons on  $|\Psi^-\rangle$ . Simultaneous events in the same output port of the BS hence  $1^H$  and  $1^V$  or in  $2^H$  and  $2^V$  indicate a projection of the photons on  $|\Psi^+\rangle$ . Like this, the atoms are projected on an entangled state.

Then one checks, whether the atom is still in the trap or has been ionized. The readout laser is aligned counterpropagating the the ODT beam.

As the readout polarization sets the basis, in which the atomic qubit is measured, one can also label the atomic states by the polarization, for which they are a dark state:

$$\begin{aligned}
 |\Psi_H\rangle &= \frac{i}{\sqrt{2}}(|1, -1\rangle - |1, 1\rangle) = |\uparrow\rangle_x \\
 |\Psi_V\rangle &= \frac{1}{\sqrt{2}}(|1, -1\rangle + |1, 1\rangle) = |\downarrow\rangle_x
 \end{aligned}
 \tag{2.12}$$

Where H and V denote horizontal and vertical linear polarization, as defined in figure A.2. Other states and corresponding readout polarizations are summarized in Table A.1.

## 2.6. Towards Longer Distances

To realize a useful quantum network, link lengths of roughly 100km are required [21]. The next goal of our experiment is to approach this order of magnitude. In this section, requirements arising for these distances will be discussed shortly.

## 2. Experimental Setup

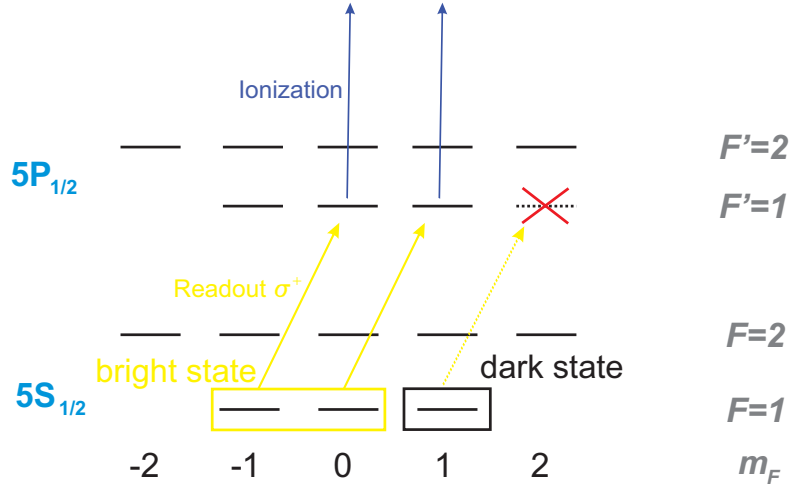


Figure 2.5.: Illustration of the Readout process

### 2.6.1. Coherence Requirements

Useful quantum networks will also require classical communication between the nodes e.g. to distribute the result of the BSM to the two nodes. Moreover, a quantum link with several nodes, via the repeater protocol, can only work, if all nodes remain coherent until the entanglement is generated between the two final nodes. In our experiment, the atomic state has to remain coherent, at least until the photon sent out has reached the BSM-setup, was detected and an electric signal was sent back to the trap. For the current setup, with a 700m fibre, this time is roughly  $7 \mu\text{s}$ , but it will grow linearly with the separation of the traps. Therefore coherence times of  $100\text{-}200\mu\text{s}$  are required in order to increase the distance to 20km. To make sure, to be well within the boundaries,  $200\mu\text{s}$  will be used in further considerations.

The minimum fidelity at  $200\mu\text{s}$  should be such, that it is still possible to violate Bell's inequality with a single link. This is a reasonable boundary, because this can never be achieved with a classical system and thus definitely proves the entanglement [5]. To violate Bell's inequality in the CHSH formulation, the so called S-value has to be larger than  $S_{low} = 2$  [10], while the maximum value is  $S_{max} = 2\sqrt{2}$ . As our system consists of 2 nodes, and S is directly proportional to the fidelity of the entire system, the minimum fidelity, of each atom  $F_{min,atm}$  has to be:

$$F_{min,atm} = \sqrt{\frac{S_{low}}{S_{max}}} \approx 84.1\% \quad (2.13)$$

For quantum communication applications and to achieve statistically significant results, actually values above 90% would be preferable. Therefore, in considerations here, the coherence time will be the time until the fidelity of the state has dropped to 90%. This limit is chosen by us for our experiment. In general a quantum network with multiple channels can work with lower fidelities in each channel. By entanglement distillation

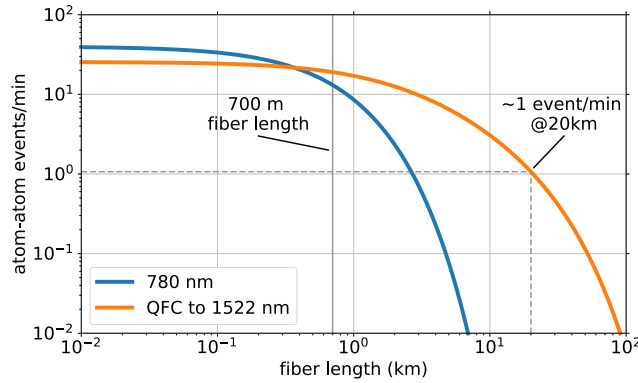


Figure 2.6.: Possible Atom-Atom entanglement event rates with and without the Quantum frequency conversion(QFC)

[37] one entangled state with high fidelity can be extracted from several states with low fidelity. But as our experiment currently only offers a single channel, these high fidelities are required.

For the Bell test measurements in 2017, the fidelity of the atom-atom state was 83% corresponding to an individual value of 91% at a delay time of  $11 \mu s$  [33]. Limitations of the fidelity will be discussed in detail in chapter 3.

### 2.6.2. Photon collection losses

The main limit on the entanglement generation rate of the experiment, is the photon collection efficiency. If the photon, emitted during the spontaneous decay, is not collected, the BSM is not possible and the atoms cannot be entangled. The photon losses consist of the photons, not being collected by the objective, and the ones, lost in the fibre.

The losses in the fibre will exponentially increase for longer distances, and for the current setup the entanglement rate will drop to almost zero for distances around 10 km (see figure 2.6). The losses in the fibre occur mainly, because the photon wavelength is 780nm and thus far away from the optimum range of commercial fibres at 1550nm. Therefore a polarization maintaining frequency conversion to this wavelength has recently been implemented and atom-photon entanglement through a 20 km fibre was verified [38]. Figure 2.6 shows the improvement in event rate, especially at large distances due to the more efficient fibre transfer.

Additionally a new objective is currently being installed, increasing the collection efficiency from 5% to 9% in each trap.

Thus the photon losses and the coherence time are currently imposing the technical limits of the quantum link. This thesis will present several approaches to increase the coherence time.



## 3. Decoherence Mechanisms

In this chapter the main decoherence effects on the atomic qubit are explained. Different parameter configurations to minimize these effects will be discussed, together with new solutions that are currently being implemented.

Section 3.1 will explain the evolution of the qubit states in a magnetic field. Section 3.2 will present certain polarization effects of the ODT, that effectively create a magnetic field around the focus. The evolution of the atomic qubit states in these, will be analysed in section 3.3. Section 3.4 will explain different ways to reduce this evolution.

### 3.1. State evolution of a spin 1 system

The atomic qubit is encoded in two Zeeman states of a spin 1 system, which obtain different energy shifts from external magnetic fields, resulting in state evolutions. The evolution of the different qubit states in an external magnetic field

$$\vec{B} = B_0 \begin{pmatrix} b_x \\ b_y \\ b_z \end{pmatrix}, \quad (3.1)$$

with the normalized components  $b_x$ ,  $b_y$ ,  $b_z$  and the magnitude  $B_0$ , can be calculated from the Hamiltonian of the system in the basis  $(|1, 1\rangle, |1, 0\rangle, |1, -1\rangle)$ :

$$\hat{H} = \frac{\mu_B g_F}{\hbar} \vec{B} \hat{F} = \begin{pmatrix} b_z & \frac{1}{\sqrt{2}}(b_x - ib_y) & 0 \\ \frac{1}{\sqrt{2}}(b_x + ib_y) & 0 & \frac{1}{\sqrt{2}}(b_x - ib_y) \\ 0 & \frac{1}{\sqrt{2}}(b_x + ib_y) & -b_z \end{pmatrix}, \quad (3.2)$$

with the Bohr magneton  $\mu_B$ , the Landé factor of the hyperfine state  $g_F$ ,  $\sqrt{b_x^2 + b_y^2 + b_z^2} = 1$ , and the angular momentum operators of a spin 1 system [24]:

$$F_x = \frac{\hbar}{\sqrt{2}} \begin{pmatrix} 0 & 1 & 0 \\ 1 & 0 & 1 \\ 0 & 1 & 0 \end{pmatrix}, F_y = \frac{\hbar}{\sqrt{2}} \begin{pmatrix} 0 & -i & 0 \\ i & 0 & -i \\ 0 & i & 0 \end{pmatrix}, F_z = \hbar \begin{pmatrix} 1 & 0 & 0 \\ 0 & 0 & 0 \\ 0 & 0 & -1 \end{pmatrix} \quad (3.3)$$

The used quantization axis is the z-axis of the coordinate system explained in Ap-

### 3. Decoherence Mechanisms

pendix A. Using cylindrical coordinates  $(b_z, \phi)$ , defined by:

$$\begin{aligned} b_x &= \sqrt{1 - b_z^2} \cos(\phi), \\ b_y &= \sqrt{1 - b_z^2} \sin(\phi), \end{aligned} \quad (3.4)$$

and the Larmor frequency  $\omega_L := \frac{1}{\hbar} g_F \mu_B B_0$  the Hamiltonian can be diagonalized with the eigenvalues  $\lambda_{\pm} = \pm \hbar \omega_L$ ,  $\lambda_0 = 0$  and eigenstates:

$$|\Phi_{\pm}\rangle = \begin{pmatrix} -\frac{1}{2}(b_z \pm 1)e^{-i\phi} \\ -\sqrt{\frac{1-b_z^2}{2}} \\ \frac{1}{2}(b_z \mp 1)e^{i\phi} \end{pmatrix}, \quad |\Phi_0\rangle = \begin{pmatrix} -\sqrt{\frac{1-b_z^2}{2}}e^{-i\phi} \\ b_z \\ \sqrt{\frac{1-b_z^2}{2}}e^{i\phi} \end{pmatrix} \quad (3.5)$$

As these form an orthogonal basis, an arbitrary state can be expressed as a superposition of them with coefficients  $c_+$ ,  $c_-$ ,  $c_0$  and will undergo a time evolution:

$$|\Psi(t)\rangle = e^{-i\hat{H}t/\hbar} |\Psi_0\rangle = c_- |\Phi_-\rangle e^{i\omega_L t} + c_0 |\Phi_0\rangle + c_+ |\Phi_+\rangle e^{-i\omega_L t} \quad (3.6)$$

To illustrate this, the time evolution of the states  $|\Psi_H\rangle$ ,  $|\Psi_V\rangle$  as defined by Equation 2.12 and  $|\Psi_0\rangle := |1, 0\rangle$  in different magnetic fields will be calculated.

#### 3.1.1. Magnetic field in x-direction

For a field in x-direction,  $\vec{B} = \begin{pmatrix} \pm B_0 \\ 0 \\ 0 \end{pmatrix}$ , hence  $b_z = 0$ ,  $\phi = 0/\pi$  and the eigenstates of the system become:

$$|\Phi_+\rangle = \frac{1}{2} \begin{pmatrix} \mp 1 \\ -\sqrt{2} \\ \mp 1 \end{pmatrix}, \quad |\Phi_-\rangle = -\frac{1}{2} \begin{pmatrix} \pm 1 \\ \sqrt{2} \\ \pm 1 \end{pmatrix}, \quad |\Phi_0\rangle = \frac{1}{\sqrt{2}} \begin{pmatrix} \mp 1 \\ 0 \\ \pm 1 \end{pmatrix} \quad (3.7)$$

and therefore

$$\begin{aligned} |\Psi_H(t)\rangle &= |\Psi_H\rangle \\ |\Psi_V(t)\rangle &= |\Psi_V\rangle \cos(\omega_L t) \pm i |\Psi_0\rangle \sin(\omega_L t) \end{aligned} \quad (3.8)$$

$|\Psi_H\rangle$  is still an eigenstate of the system, but  $|\Psi_V\rangle$  will rotate into  $|\Psi_0\rangle$  and back with the larmor frequency.

### 3.1.2. Magnetic field in y-direction

For a field in y-direction,  $\vec{B} = \begin{pmatrix} 0 \\ \pm B_0 \\ 0 \end{pmatrix}$ , hence  $b_z = 0, \phi = \pm \frac{\pi}{2}$  and the eigenstates of the system become:

$$|\Phi_+\rangle = \frac{1}{2} \begin{pmatrix} \pm i \\ \sqrt{2} \\ \mp i \end{pmatrix}, |\Phi_-\rangle = \frac{1}{2} \begin{pmatrix} \mp i \\ -\sqrt{2} \\ \pm i \end{pmatrix}, |\Phi_0\rangle = \frac{1}{\sqrt{2}} \begin{pmatrix} \pm i \\ 0 \\ \pm i \end{pmatrix} \quad (3.9)$$

and therefore

$$\begin{aligned} |\Psi_H(t)\rangle &= |\Psi_H\rangle \cos(\omega_L t) \mp i |\Psi_0\rangle \sin(\omega_L t) \\ |\Psi_V(t)\rangle &= |\Psi_V\rangle \end{aligned} \quad (3.10)$$

$|\Psi_V\rangle$  is still an eigenstate of the system, but  $|\Psi_H\rangle$  will rotate into  $|\Psi_0\rangle$  and back with the larmor frequency.

### 3.1.3. Magnetic field in z-direction

For a field in z-direction,  $\vec{B} = \begin{pmatrix} 0 \\ 0 \\ \pm B_0 \end{pmatrix}$ , hence  $b_z = \pm 1, \phi = 0$  and the eigenstates of the system become:

$$|\Phi_+\rangle = -\frac{1}{2} \begin{pmatrix} 1 \pm 1 \\ 0 \\ 1 \mp 1 \end{pmatrix}, |\Phi_-\rangle = \frac{1}{2} \begin{pmatrix} 1 \mp 1 \\ 0 \\ 1 \pm 1 \end{pmatrix}, |\Phi_0\rangle = \begin{pmatrix} 0 \\ \pm 1 \\ 0 \end{pmatrix} \quad (3.11)$$

and therefore

$$\begin{aligned} |\Psi_H(t)\rangle &= |\Psi_H\rangle \cos(\omega_L t) \pm |\Psi_V\rangle \sin(\omega_L t) \\ |\Psi_V(t)\rangle &= |\Psi_V\rangle \cos(\omega_L t) \mp |\Psi_H\rangle \sin(\omega_L t) \end{aligned} \quad (3.12)$$

Neither  $|\Psi_V\rangle$  nor  $|\Psi_H\rangle$  is an eigenstate of the system. They will both rotate into each other, and back.

Figure 3.1 illustrates the situation for different magnetic fields.

### 3. Decoherence Mechanisms

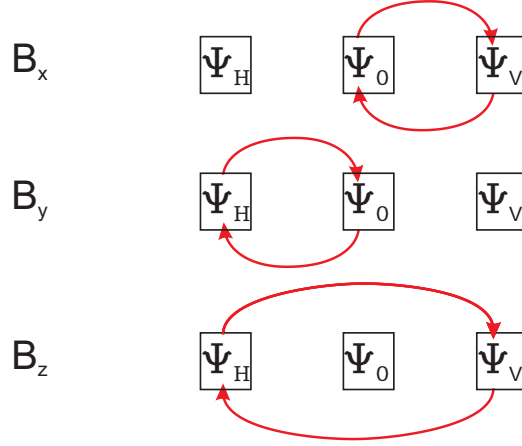


Figure 3.1.: Illustration of the state evolution in different magnetic fields

#### 3.1.4. Circular Dipole Trap Polarization

As mentioned in section 2.2.2, circular polarization of the ODT results in a different potential depth for each  $m_F$  state. The energy shift of each state relative to the  $m_F = 0$  state can be calculated from equation 2.1:

$$\Delta E_{m_F}(\vec{r}) = -\frac{\pi c^2}{2} \frac{\Gamma}{\omega_0^3} \left( -\frac{P g_F m_F}{\delta_{1F}} + \frac{P g_F m_F}{\delta_{2F}} \right) \cdot I(\vec{r}), \quad (3.13)$$

with  $\delta_{1,F}$  and  $\delta_{2,F}$  the detunings to the  $D_1$  and  $D_2$  line, the circularity of the light  $P$ , as defined in Appendix B. Expressing it by the potential seen by every state equally  $U(\vec{r})$  (equation 2.5) yields [9]:

$$\Delta E_{m_F}(\vec{r}) = R_{circ} g_F m_F P \cdot U(\vec{r}), \quad (3.14)$$

with  $R_{circ} = \frac{\delta_{1,F} - \delta_{2,F}}{2\delta_{1,F} + \delta_{2,F}}$ . This energy shift is equivalent to the Zeeman effect of a magnetic field pointing in propagation direction of the beam [11], defined as:

$$\vec{B}_{eff}(\vec{r}) = \frac{\Delta E_{m_F}(\vec{r})}{\mu_B} \vec{e}_z \quad (3.15)$$

The description in terms of this effective magnetic field will be used in the following considerations, as it allows to compare the effects of circular polarization and external magnetic fields on the atomic states.

Mind that all state evolutions described in this and the previous sections are coherent processes, that do not limit the fidelity. Considering a magnetic field of known strength, one can measure the state after an arbitrary number of full larmor rotations and will obtain the input state.

## 3.2. Polarization Effects of a Strongly Focussed ODT

The formalism of Gaussian optics as described in section 2.2.2, is a powerful tool, for a wide range of parameters. However due to the paraxial approximation, it is not valid for beams focussed to several  $\mu m$  waist because of their large divergence. In these cases, the polarisation of the beam influences its shape and vice versa.

Since the ODT is tightly focussed it is important to further investigate the deviations from Gaussian optics in this case. Richards, Bovin and Wolf derived exact diffraction integrals to calculate the electric fields in the vicinity of the focus of a linear polarized plane wave, created by a lens with focal length  $f$  [7][3]. We followed these derivations, with the extension that a collimated Gaussian beam was used as input [32]. This yields the components of the electric field in the vicinity of the focus:

$$\begin{aligned} \mathcal{E}_x(r, \phi, z) &= \mathcal{E}_0 \cdot (F_0(r, z) + F_2(r, z) \cos(2\phi)) \\ \mathcal{E}_y(r, \phi, z) &= \mathcal{E}_0 \cdot F_2(r, z) \sin(2\phi) \\ \mathcal{E}_z(r, \phi, z) &= \mathcal{E}_0 \cdot 2iF_1(r, z) \cos(\phi) \end{aligned} \quad , \quad (3.16)$$

with the coordinate system as defined in Appendix A,  $\mathcal{E}_0$  the electric fields amplitude and the diffraction integrals:

$$\begin{aligned} F_0(r, z) &= \int_0^\alpha d\theta \exp\left(\frac{-f^2 \tan(\theta)^2}{w(f)^2}\right) \sqrt{\cos(\theta)} (1 + \cos(\theta)) J_0(kr \sin(\theta)) e^{ikz \cos(\theta)} \sin(\theta), \\ F_1(r, z) &= \int_0^\alpha d\theta \exp\left(\frac{-f^2 \tan(\theta)^2}{w(f)^2}\right) \sqrt{\cos(\theta)} \sin(\theta) J_1(kr \sin(\theta)) e^{ikz \cos(\theta)} \sin(\theta), \\ F_2(r, z) &= \int_0^\alpha d\theta \exp\left(\frac{-f^2 \tan(\theta)^2}{w(f)^2}\right) \sqrt{\cos(\theta)} (1 - \cos(\theta)) J_2(kr \sin(\theta)) e^{ikz \cos(\theta)} \sin(\theta), \end{aligned} \quad (3.17)$$

with the waist expected from Gaussian optics at the position of the lens  $w(f)$  and  $J_0, J_1, J_2$  being the Bessel-J functions of the first kind. The integrals sum waves from infinitesimal rings in the lens plane, with the opening angle  $\theta$  seen from the integration point, up to the aperture of the lens  $\alpha$ .  $F_2$  slightly changes the focus sizes in x- and y-direction, however for waists larger than  $1\mu m$  these changes are negligible, since it is more than an order of magnitude smaller than  $F_2$  or  $F_1$ . In this range,  $F_0$  and  $F_1$  can

### 3. Decoherence Mechanisms

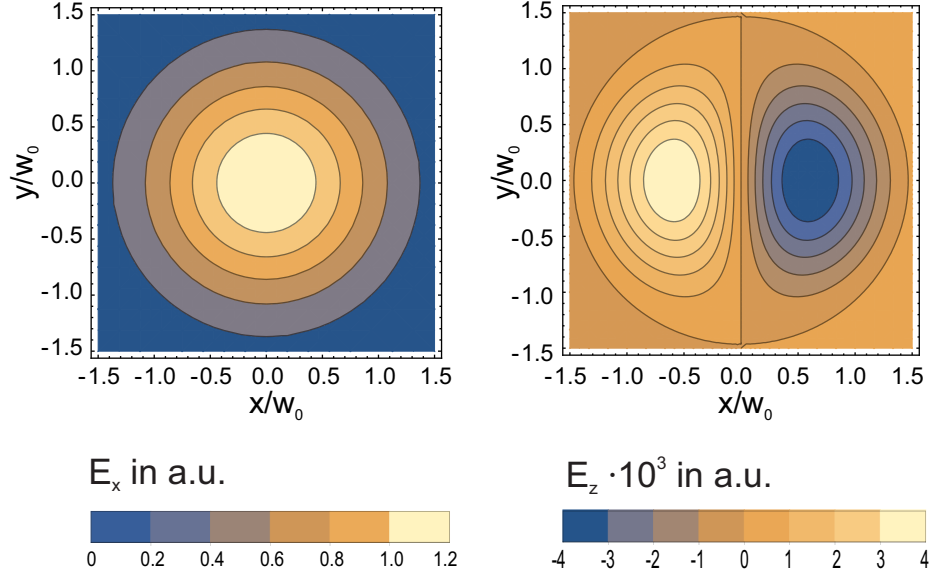


Figure 3.2.: Real part of the x and y component of the electric field in the focal plane ( $z=0$ ). Mind the factor of  $10^3$  between the amplitudes

also be approximated such, that  $\mathcal{E}_x$  and  $\mathcal{E}_z$  have the field distribution of the  $TEM_{00}$  and the  $TEM_{01}$  mode [32]. Therefore, the field distribution of  $\mathcal{E}_x$ , as given in equation 2.2 is still valid, while:

$$\mathcal{E}_z(\vec{r}) = \mathcal{E}_0 \cdot \frac{i}{z_R} \frac{x}{1 + \frac{z^2}{z_R^2}} \exp\left(-\frac{x^2 + y^2}{w(z)^2} + i\varphi_{01}(\vec{r})\right) \quad (3.18)$$

with the definitions for the Gaussian beam as in equation 2.2 and:

$$\varphi_{01}(\vec{r}) = \omega t + kz + k \frac{x^2 + y^2}{2R} - 2 \arctan\left(\frac{z}{z_R}\right). \quad (3.19)$$

Surprisingly, the light field of the focussed beam gets off axis a longitudinal polarisation component near the focus, that is propagating in the  $TEM_{01}$  mode. This can be understood intuitively, by the fact that the linear polarization vector, that is perpendicular to the propagation direction, gets slightly tilted because of the strong divergence. Resulting in a longitudinal component with different sign on both sides of the  $x=0$  plane. That is why the  $\mathcal{E}_z$  component is in the  $TEM_{01}$  mode, while the transverse polarization is still propagating in  $TEM_{00}$ . Figure 3.2 shows the distribution of the electric field amplitudes in the transversal plane at the focus position.

The factor  $i$  in equation 3.18 for  $\mathcal{E}_z$  corresponds to a  $\frac{\pi}{2}$  phase shift, that ensures that

### 3.2. Polarization Effects of a Strongly Focussed ODT

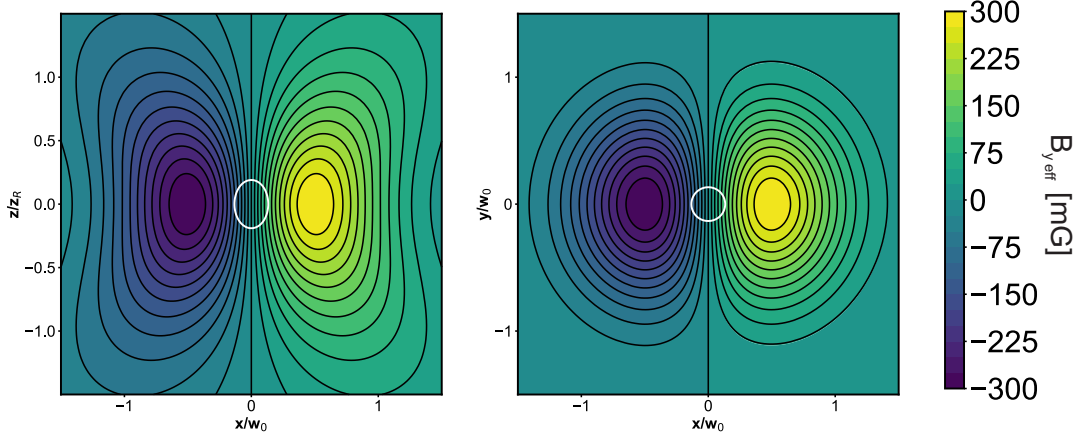


Figure 3.3.: Effective magnetic field of the ODT for  $w_0 = 1.9\mu m$ ,  $U_0=2.7mK$ , in the  $xz$ -plane (left) and  $xy$ -plane(right). White ellipses show the area within which the probability to find a  $T_{atm}=50\mu K$  atom is 95 %.

the  $\mathcal{E}_x$  and  $\mathcal{E}_z$  components start in phase in the far field, although the Gouy phase of the  $\mathcal{E}_z$  component has a factor of 2 relative to the  $\mathcal{E}_x$  component. Therefore, there is a phase difference between the two components of the polarisation, that can be written as:  $\delta = \arctan\left(\frac{z}{z_R}\right) + \frac{\pi}{2}$ . This results in a phase shift of exactly  $\frac{\pi}{2}$  in the focus. Therefore, the tightly focussed ODT beam propagating in  $z$ -direction will produce an electric field like an elliptically polarized beam propagating in  $y$ -direction (see Appendix B). As the  $TEM_{01}$  mode has a phase difference of  $\pi$  between the two nodes on each side of the beam, the elliptical polarizations on both sides of the beam, rotate in different directions.

As described in 3.1.4 the effect of circular polarization in the ODT on the atomic state is the same as the Zeeman shift of a magnetic field pointing in propagation direction. Therefore, the polarization effects due to the strong focussing can be treated as an effective magnetic field in  $y$  direction, defined as in equation 3.15:

$$B_{y,eff}(\vec{r}) = \frac{R_{circ}}{\mu_B} \cdot P \cdot U(\vec{r}) \quad (3.20)$$

with  $R_{circ}$  as defined in section 3.1.4,  $P$  as explained in Appendix B, and the potential of the dipole trap as defined in equation 2.5. Mind that also  $P$  has a dependency on the position. The spatial distribution of this effective magnetic field is shown in figure 3.3

### 3.3. Evolution of the Atomic State in the Effective ODT field

After preparing an atom in a certain state, the atom will oscillate in the trap. Along its trajectory, the atom sees different fields at each position, and since the atomic state is prepared at a random position, all state evolutions are unique. When averaging over many experimental runs, this causes a quick dephasing of the atomic state, on the time scale of the trap frequency [9].

Luckily, rephasing to the prepared state occurs, since the trap is highly elliptical, due to the Gaussian shape of the potential. Therefore, the longitudinal oscillations of the atom, are much slower than the transversal and the effective field is antisymmetric with respect to the  $z$ -axis. So an atom moving back and forth in one transversal oscillation will see the same fields on both sides of the  $z$ -axis, but with a different sign. Therefore, the state will also evolve back and forth equally for all initial conditions. This causes rephasing after one oscillation period, such that atoms will always be back in the initially prepared state after one oscillation period of its movement in the trap.

This rephasing process is limited by three facts:

Firstly the trap potential is not harmonic but Gaussian. Therefore atoms with different kinetic energies have different oscillation periods. As energy of the atom is thermally distributed the exact rephasing time cannot be known, and a measurement will be an average over many atomic trajectories. Also the trap frequency will slightly vary for different  $z$ -positions (see equation 2.2.2). This error will accumulate for longer waiting times, because the rephasing times of different atoms will spread out more and more, resulting on average in a reduced fidelity at later rephasing points.

Secondly, the atom also oscillates along the optical axis, and therefore does not see exactly the same fields during one transversal oscillation. This effect is minimal for one oscillation, but it will also accumulate for a higher number of oscillation periods. However it is independent of the duration of one oscillation.

Thirdly, the fields may not be exactly symmetric on both sides of the beam. Imperfect alignment of the ODT beam to the objective, will introduce asymmetries in the focus, resulting in slightly different fields on both sides of the beam.

The resulting evolution of the atomic state is shown in figure 3.4.

#### 3.3.1. Simulation

Figure 3.4 shows the evolution of two different state populations with measured points and the graph from a simulation. The simulation takes random initial positions and velocities from a thermal distribution with temperature  $T_{atm}$  in the ODT potential and simulates the resulting trajectory with a high temporal resolution. Then the evolution of four different initial states is calculated by evaluating the approximated expression for the effective magnetic field (equation: 3.20, with 3.18) at every point of the trajectory, deriving a Larmor precession for every time step and applying that rotation on the atomic state. This is done for up to 20 000 trajectories and finally the state evolution is averaged

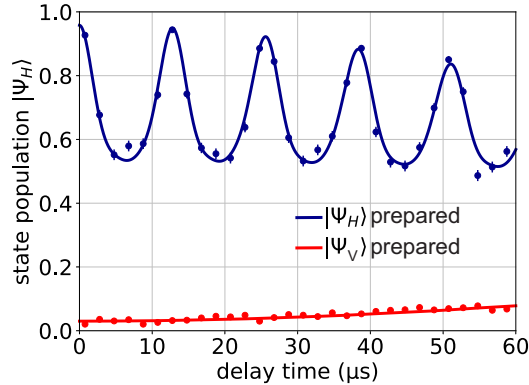


Figure 3.4.: Evolution of the state population in the effective fields of the ODT simulated (lines) and measured (points).  $\Psi_V$  is not affected by the effective  $B_y$  field (see section 3.1)  $U_0 = k_B \cdot 3.2\text{mK}$ ,  $T_{atm} = 45\mu\text{K}$ ,  $w_0 = 1.9\ \mu\text{m}$ )

over these.

The simulation also takes fluctuations of the external magnetic field into account. These occur due to imperfections in the compensation of external fields and the control of the magnetic coils. These fluctuations are assumed to be Gaussian distributed, with standard deviations measured in [23]. In the simulation, they are implemented by adding a random value from the given distribution to the magnetic field. This value is constant during one trajectory, as these fluctuations are on a much slower time scale.

The measurement points in figure 3.4 are taken by preparing one atom in either  $\Psi_H$  or  $\Psi_V$ , by measuring the emitted photon in the HV-basis and then reading out the atomic state with  $\Psi_H$  as a dark state after a certain delay time. To get the state population, many atoms are measured and the average is taken.

### 3.3.2. Parameter configuration for the Bell Test

For the loophole free Bell Test, a high fidelity in both traps at the same time was required, as the state readout has to be done simultaneously. Therefore, the first rephasing points of both traps had to be the same. As trap 2 has a communication time of  $3.6\mu\text{s}$  to trap 1 and the BSM (see section 2.4.2), the depth of trap 2 was chosen lower, resulting in a lower trap frequency. As the first rephasing time of trap 1 was limited to  $11\mu\text{s}$  by the laser power, the frequency of trap 2 was chosen to be  $14.5\ \mu\text{s}$  corresponding to  $k_B \cdot 3.2\text{mK}$  and  $k_B \cdot 1.8\text{mK}$  trap depth.

In order to achieve a maximum event rate of atom-atom entanglement the protocol sketched in figure 3.5 was implemented. It is designed to overcome the following challenges: Firstly, the photon collection and BSM has a very low success probability of only  $\eta = 7 \cdot 10^{-7}$  to give a two photon event, from one excitation try [9]. Therefore multiple excitation tries are required, before one atom-atom entanglement is generated. Secondly, the atom is heated during the excitations and state preparations by optical

### 3. Decoherence Mechanisms

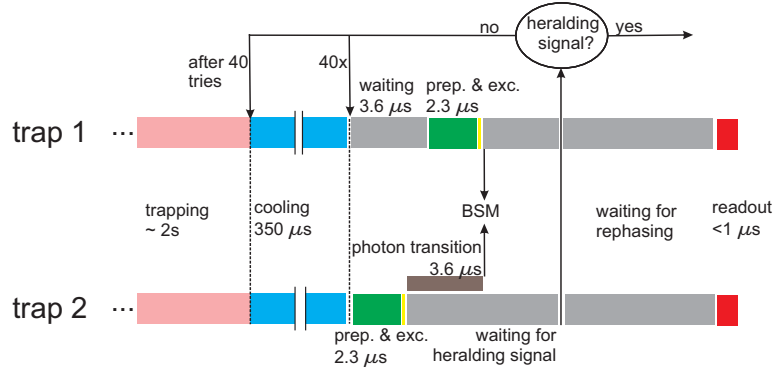


Figure 3.5.: Illustration of the timing scheme, used during the Bell-test

pumping. Therefore, it needs to be cooled after several tries. Thirdly, the readout of the atomic states has to be at the same time in both traps, to close the locality loophole.

Thus, after both atoms are cooled and loaded into the ODT, 40 excitations are performed, whereby the atom in trap 1 is always excited 3.6 μs later. After each excitation step both traps wait for a heralding signal from the BSM to arrive. For trap 2, this also takes 3.7 μs. If the BSM is successful, both traps wait until the atoms have rephased and then read out the atomic state in a set basis. The trap parameters are chosen such, that this will happen at the same time for both traps. If the BSM does not give a heralding signal, another excitation attempt is performed in both traps. After 40 excitation tries, a cooling period of 350 μs is applied. If the atom is lost due to the destructive readout or thermal movement, a new atom is loaded, before the protocol is continued.

Altogether this yields an excitation rate of  $52.2 \cdot 10^3 \frac{1}{s}$ , and 2.2 atom-atom entanglements per minute. This will be increased with more efficient photon collection optics by a factor of 4 (see 2.6.2).

### 3.4. Increasing the coherence Time

Currently the atom traps are separated by 400 meters, which results in a communication time of 7 μs. When increasing the distance between the atoms this time will grow linearly. Decoherence induced by magnetic or optical fields should be eliminated entirely to reach distances above 10 km. The effects of optically induced fields can be eliminated entirely by using a standing wave dipole trap. This approach is explained in detail in chapter 4. In this section, methods to reduce different decoherence effects of the atomic state are presented. Most of them will also be required in combination with a standing wave trap, to suppress residual fluctuations of the ambient magnetic field.

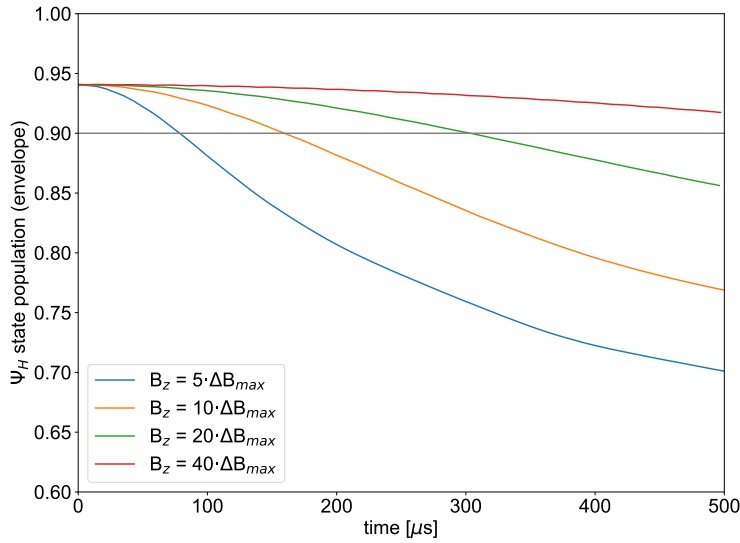


Figure 3.6.: Simulated evolutions of the population of the state  $\Psi_H$ , with gaussian distributed magnetic field fluctuations in x- and y-direction with standard deviation  $\sigma = \frac{\Delta B_{max}}{2} = 10\text{mG}$  and a guiding field in z-direction. Fluctuations along the z-axis are turned off. As the guiding field introduces fast oscillations to the state evolution, only the envelopes are shown.

### 3.4.1. Magnetic Guiding Field

When applying a bias magnetic field, the influence of small fluctuations perpendicular to this field is suppressed and the direction of the total magnetic field vector will be approximately along the bias field. Hence the state evolution is mainly defined by the guiding field and one can achieve higher fidelities, by measuring the state after an integer number of larmor rotations [27].

Fluctuations parallel to the guiding field, will still change the fields amplitude and therefore the frequency of the larmor precession.

Without fluctuations along the guiding field, the possible coherence times, achievable with this method are limited by the ratio of the guiding fields strength to the amplitude of the fluctuations. Figure 3.6 shows the evolution of the state population for different guiding field strengths. The curves are calculated without fluctuations parallel to the guiding field, to show the ideal case, when these are eliminated by other means, which will be described in section 3.4.3. Currently residual fluctuations of the ambient magnetic field in the experiment are gaussian distributed with a standard deviation of 0.3 mG [23]. The ratio of these to the guiding field will finally limit the coherence time, when all other magnetic effects are eliminated. A guiding field roughly 10 times stronger than the fluctuations will keep the loss introduced by decoherence below 5 % for 200  $\mu\text{s}$ . Note that when the fluctuations are of the same order of magnitude as the guiding field, the guiding field even reduces the fidelity.

### 3. Decoherence Mechanisms

In the current trap setup, various effects limit the maximum guiding field. Firstly, the Larmor precession induced by the guiding field has to be much slower than the state readout, which takes 160 ns. A state contrast of more than 99 %, averaged over the readout time, requires a minimal larmor precession time of  $2 \mu\text{s}$ , corresponding to a guiding field of maximally 350mG. Secondly, the polarization gradient cooling will become less efficient when a magnetic field is applied, resulting in higher atomic temperatures [14]. Thirdly, for the initial state preparation by optical pumping, the  $m_F=0$  ground state should be a dark state [40], which is not the case if a magnetic field in x- or y-direction is present (see section 3.1). Significant changes in the state preparation efficiency were found experimentally for magnetic fields above 50 mG in these directions. Therefore, this is the maximum usable magnetic field in these directions.

For these reasons, we limit the guiding field to 250mG in z-direction enabling suppression of fluctuations up to 25mG in x- and y-direction during coherence times up to  $200 \mu\text{s}$ .

#### 3.4.2. Lower Atomic Temperature and Potential Depth

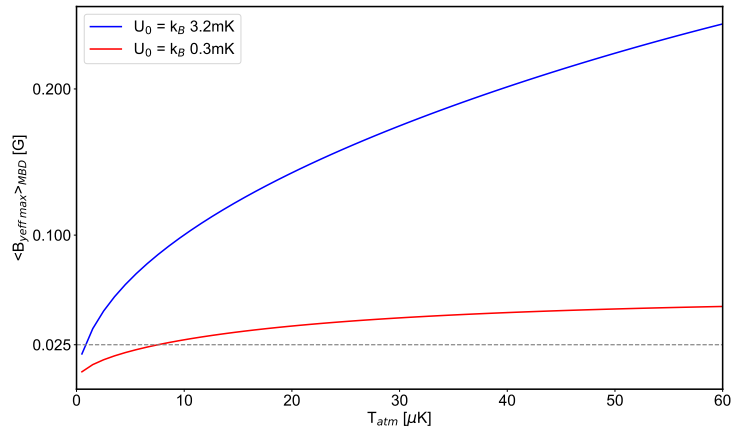


Figure 3.7.: Averaged differences in  $B_{y,eff}$  the atom sees as defined in the text at different temperatures  $T_{atm}$  for two different trap depths. The maximum difference the guiding field can suppress is 25mG (grey line).

As the effective field of the ODT is proportional to the laser intensity, lowering the trap depth results in lower optically induced effective magnetic fields. However, in the shallower trap, it also becomes more likely for the atom to leave the trap because of thermal movement. Additionally the atom is heated, during the entanglement generation process. For too shallow trap depths, this heating can be enough to kick the atom out of the potential, causing the experimental procedure to abort.

For this reason, the atom also has to be cooled more when lowering the trap depth, resulting in a lower repetition rate of the entanglement generation.

Figure 3.7 shows  $\langle \Delta B_{y,eff} \rangle_{MBD}$ , the maximum difference in effective magnetic field an atom will see, averaged over the Maxwell-Boltzmann distribution (MBD), for different temperatures of the atom. During the Bell-test experiments  $U_0 = 3.2mK$ , and  $T_{atm} \approx 45\mu K$  were used. The figure shows, that by ramping down the trap depth to  $0.3mK$  and cooling the atom to around  $8\mu K$  one can achieve field fluctuations, that can be suppressed with a guiding field of  $250mG$ . This was achieved by adding cooling periods to the protocol in figure 3.5 and ramping down the trap adiabatically, what reduced the atom temperature even further.

Because of the additional cooling periods, the repetition rate of the experiment dropped by a factor of 4 to less than one event per minute. Therefore, this method is not suited for an applicable quantum network link.

### 3.4.3. State Transfer

By lowering the trap depth and applying a magnetic guiding field in z-direction, decoherence due to magnetic fluctuations in x and y direction can be suppressed, but the qubit is still sensitive to magnetic fluctuations along the guiding field. This can be addressed by a Zeeman selective state transfer, to a basis that is less sensitive to magnetic fluctuations along the z-axis [27].

In our experiment, this can be achieved via transferring the population in the  $F=1$   $m_F=+1$  state to the  $F=2$ ,  $m_F=1$  state, forming the new basis  $|1, -1\rangle$ ,  $|2, 1\rangle$  as shown in figure 3.8. The relative energy shift in a magnetic field along the z-axis  $B_z$  of these two states can be calculated as:

$$\Delta E = \Delta_{hf} + 2g_I \mu_B B_z, \quad (3.21)$$

with the hyperfine splitting of  $^{87}Rb$   $\Delta_{hf} \approx \hbar \cdot 6.8GHz$ , the nuclear factor  $g_I$ , and the Bohr magneton  $\mu_B$  [27]. Hence the sensitivity to magnetic fields in z-direction of the new basis is reduced by the factor  $\frac{g_I}{g_F} \approx 1/504.8$ .

The state is transferred by a stimulated Raman transition with two  $\sigma^\pm$  polarised photons, blue detuned to the transition to the  $5P_{1/2}$   $F'=2$  manifold. The Zeeman state selectivity is realised, by the guiding field in z-direction, shifting the  $m_F$  states of the ground-level  $F=1$  and  $F=2$  manifolds such that only the transfer of the  $F=1$   $m_F=+1$  state will be in resonance with the difference frequency of the two laser fields. The state is transferred back to the qubit basis ( $F=1$ ,  $m_F = \pm 1$ ) just before the readout. Figure 3.8 illustrates the transfer.

This scheme is currently being implemented, achieving transfer efficiencies of around 98%.

### 3. Decoherence Mechanisms

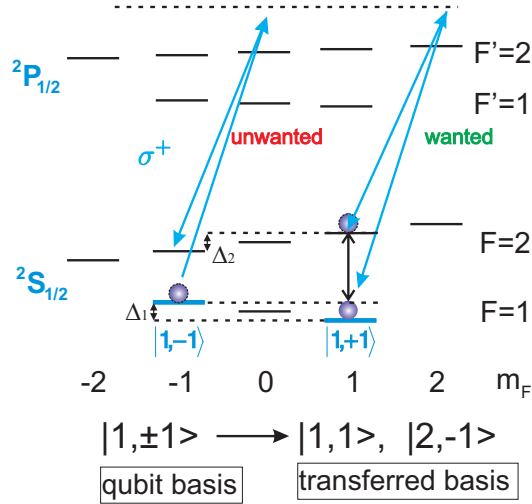


Figure 3.8.: Level scheme of the stimulated Raman transition for the state transfer. The Zeeman state selectivity is achieved by the detuning  $\Delta_1 + \Delta_2$  of the unwanted transition.

#### 3.4.4. Summary

Figure 3.9 summarizes the effect of the different presented methods on the state evolution.

A lower ODT and more cooling can never produce coherence times longer than  $100\mu\text{s}$  even if the effective field of the ODT was not present (see blue curve in figure 3.9, top left). Cooling the atom more reduces the amplitude of the de- and rephasing process (see also figure 3.4), but can not suppress it completely. A lower ODT results in lower trap frequencies, therefore the rephasing oscillations get slower. Interestingly, the amplitude is hardly affected by this. Apparently the slower oscillations of the atom, in the weaker fields introduce the same amount of state rotation as the faster oscillations in the stronger fields (compare blue and red curves in figure 3.9 top left).

A guiding field of 250mG can suppress the effect of ambient magnetic fluctuations in x- and y-direction, but not the effective fields of a high ODT. By cooling the atom to  $8\mu\text{K}$ , coherence times of up to  $140\mu\text{s}$  can be achieved (see Figure 3.9, b).

By adding the state transfer, also magnetic fluctuations in z-direction can be suppressed by a factor of 500, resulting in coherence times of more than  $250\mu\text{s}$  if the atom is cool enough (see Figure 3.9, c).

The effect of ramping down the trap, cooling more, a guiding field and the state transfer on the state contrast after  $200\mu\text{s}$  is summarized in figure 3.10. It is clearly visible, that for very low temperatures and trap depths, more than 90% contrast can be achieved.

Unfortunately, as mentioned before, ramping down the trap and additional cooling decreased the rate of atom-atom entanglement. Therefore other techniques to reduce

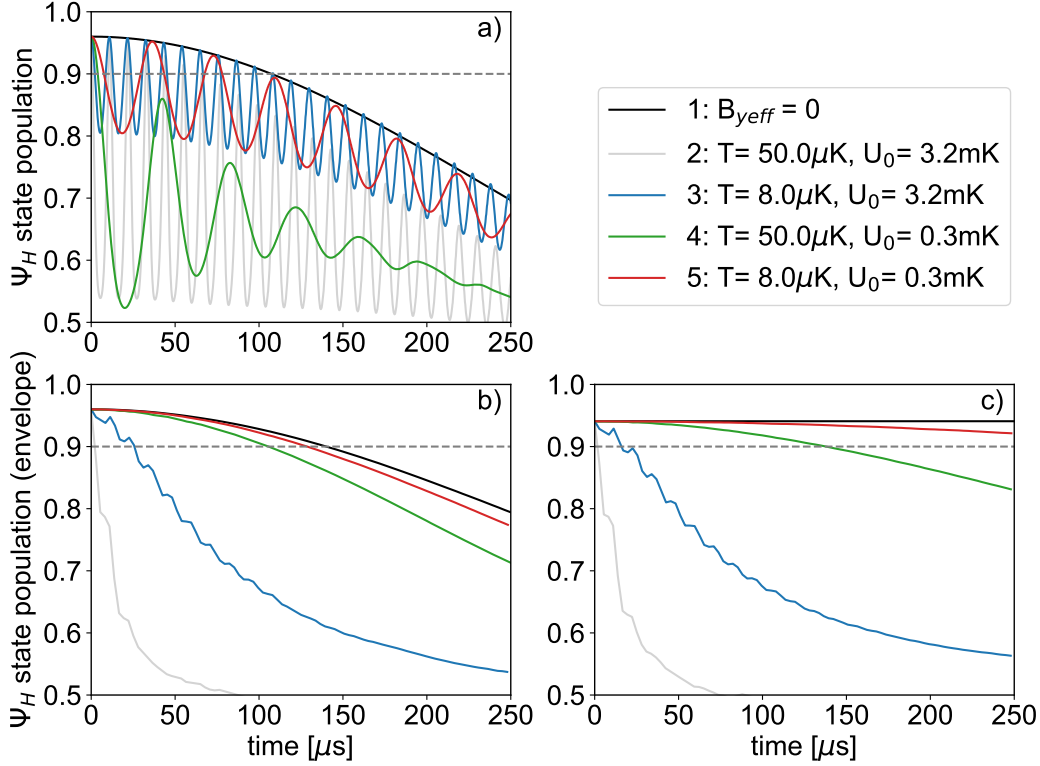


Figure 3.9.: Simulated evolutions of the state population if  $\Psi_H$  is prepared with different trap parameter configurations. Without a guiding field (a), with a guiding field  $B_z=250$  mG (b), with guiding field and state transfer (c). As the guiding field introduces fast oscillations (b) and (c) show only the envelope of the curves. The black curves show the state evolution without any optically induced effective magnetic fields.

### 3. Decoherence Mechanisms

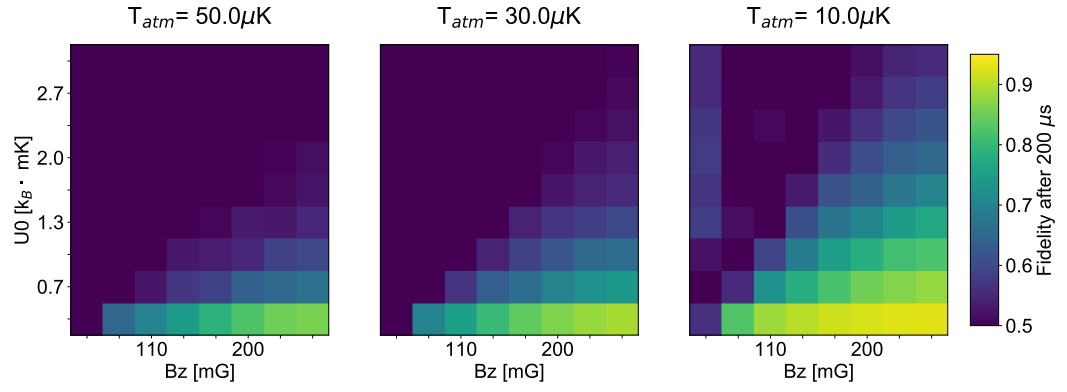


Figure 3.10.: Fidelity after 200  $\mu\text{s}$  with successful state transfer, when varying the guiding field and the trap depth for three different atom temperatures. Mind that for  $T_{atm} = 50 \mu\text{K}$  and the lowest trap depths the atom will probably be lost during the entanglement generation.

the effective magnetic fields to less than 25mG are required. This can be provided by a standing wave dipole trap, as presented in chapter 4.

## 4. Standing Wave Dipole Trap

As explained in section 3.4, a guiding field of 250 mG in z-direction in combination with a state transfer, can eliminate the effect of all magnetic fluctuations smaller than 25 mG, on the coherence time of the atomic qubit. This leaves the effective fields of the ODT as the currently largest source of decoherence. As presented in section 3.4 they can be reduced to 25mG at the cost of repetition rate due to ramping down the ODT depth and prolonged cooling periods. In order to avoid this, a standing wave can be used. As the effective fields have a different sign on both sides of the beam (see figure 3.3) they cancel, if a perfectly aligned, counter-propagating beam is used.

This chapter will explain this approach. The idea how to implement it in the setup is to split the ODT-beam with a single mode fibre BS and use these two beams to ensure a stable phase relation up to path length fluctuations and the same wavelength. Both beams will be focussed with identical high NA objectives, collimated again by the objective of the counter propagating beam and guided to the fibre coupler of the other beam. In order to ensure good spatial overlap, fibre back-coupling into the fibre of the other beam will be used as criterion. The setup is sketched in figure 4.1.

Section 4.1 will explain the new geometry of the ODT potential, in the standing wave configuration. Section 4.2 will explain how exactly the effective fields will cancel. Section 4.3 will discuss the effect of different misalignments of the beams on the effective fields and show the effect of the residual fields on the atomic state. Section 4.4 will explain how the atom can be centred inside the trap and section 4.5 will shortly present a protocol how to load an atom in the new trap and estimate its duration.

The planned experimental setup, requirements and corresponding tests will be discussed in chapter 5.

### 4.1. Geometry of a Standing Wave Dipole Trap

An additional, counter propagating ODT-beam, results in a spatial modulation of the light field intensity. In order to describe the modulation mathematically, the electric field of a second Gaussian beam propagating in positive z-direction is added to the field in Equation 2.2. Ideally, the counter-propagating field is also H polarised and therefore described by exactly the same expressions as the original beam, with the only difference:  $z \rightarrow -z$ , . This results for the x component of the composed electric field in:

#### 4. Standing Wave Dipole Trap

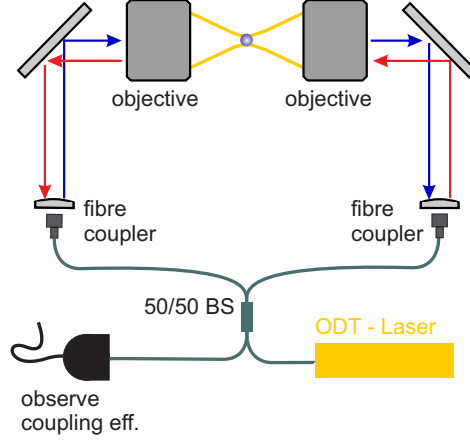


Figure 4.1.: Schematic of the planned standing wave dipole trap setup. The beams will be aligned by optimizing the coupling efficiency into the out-coupler of the counter-propagating light field, which is monitored at the observe coupling efficiency port. Further details can be found in chapter 5.

$$\begin{aligned} \mathcal{E}_x(\vec{r}) = & \mathcal{E}_0 \frac{w_0}{w(z)} \cdot \exp\left(-\frac{r^2}{w(z)^2} + i\omega t + i\frac{\Delta\varphi}{2}\right) \\ & \cdot 2 \cos\left(kz + k\frac{r^2}{2R} - \arctan\left(\frac{z}{z_R}\right) - \frac{\Delta\varphi}{2}\right), \end{aligned} \quad (4.1)$$

with all definitions as in section 2.2.2,  $r = x^2 + y^2$ , in the coordinate system as defined in Appendix A and  $\Delta\varphi$ , the phase difference between the two beams. For equal intensity, equal polarization and perfect alignment, this yields the following potential:

$$\begin{aligned} U_{SW}(x) = & -U_{0SW} \cdot I_N(\vec{r}) \\ = & -U_{0SW} \frac{1}{1 + \left(\frac{z}{z_R}\right)^2} e^{-\frac{2r^2}{w(z)^2}} \cdot \cos^2\left[kz + k\frac{r^2}{2R} - \arctan\left(\frac{z}{z_R}\right) - \frac{\Delta\varphi}{2}\right], \end{aligned} \quad (4.2)$$

with the normalized intensity distribution  $I_N$ , where like in section 2.2.2 all constant factors have been absorbed into  $U_{0SW}$ , which is the maximum potential depth. Mind that overlapping two beams, with both the intensity to create a potential of depth  $U_0$  on their own will result in  $U_{0SW} = 4U_0$ .

$U_{SW}(x)$  is the effective potential of the running wave (RW) trap (see Equation 2.5), modulated with the cosine-term. This introduces a pocket structure in  $z$ -direction, splitting the potential into pockets with a spacing of  $\frac{\lambda}{2}$ . The other phase terms in the

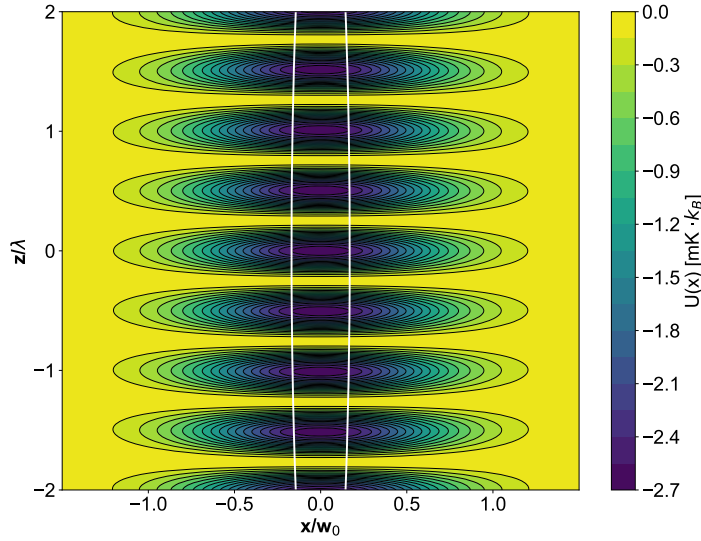


Figure 4.2.: Potential of the SW trap with  $U_{0SW} = k_B \cdot 2.7 \text{mK}$ . White ellipse shows the furthest points 95 % of all  $T = 50 \mu\text{K}$  atoms can reach in a RW trap of same depth, corresponding to 15 pockets of the SW trap.

cosine cause deformations of the outer pockets. Changing the phase difference between the beams  $\Delta\varphi$  moves the pockets along the optical axis. In this way, once the atom is trapped in one pocket, it can be moved by changing the relative phase of the beams. If this phase varies randomly, the pockets will shake with the respective frequency, which leads to heating or even loss of the atom. Therefore, active control and stabilisation of the phase difference between the beams is desired.

Figure 4.2 shows the potential of the SW trap, together with the area, where 95% of the  $50 \mu\text{K}$  atoms would be in a RW-trap of half the depth. By first turning on one beam, the collisional blockade effects ensures loading of a single atom [34]. Then the second beam will be ramped up slowly compared to the trap frequencies, trapping the atom in one of the pockets that lie within the white ellipse in figure 4.2. For the sketched example these would be the central 22 pockets. In general, the furthest point 95% of all atoms can reach is calculated from solving  $U(0,0,z) = U_0 + E_{95}$  as:

$$z_{max} = z_R \sqrt{\frac{E_{95}}{U_0 - E_{95}}}, \quad (4.3)$$

with the Rayleigh-length  $z_R$  and  $E_{95} = -\ln(1 - 0.95)k_B T$  is the energy where the integral of the Boltzmann distribution reaches 0.95. The number of pockets, is given by this distance, divided by  $\frac{\lambda}{2}$ . Analogously, in the following, the confinement area will be used. It is defined as the area, where the potential depth is lower than  $E_{95}$ .

#### 4. Standing Wave Dipole Trap

In the SW trap, the atom will now be confined most tightly in z-direction, while this was the loosest direction in the RW trap. An approximate expression for the new trap frequency in longitudinal direction can be found by approximating the expression  $U_{0SW} \cdot \cos^2(kz)$  to second order [16]:

$$\omega_L = \sqrt{\frac{2U_{0SW}k^2}{m}} = 2\pi \cdot 12.6...41.0 \text{ MHz}. \quad (4.4)$$

The potential in the transversal plane is not affected by the second beam.

### 4.2. Elimination of Circular Polarisation

The expression for the longitudinal component of the polarization of the counter-propagating beam is also very similar to the one derived in section 3.2. Again like in the x-component  $z$  is replaced by  $-z$  but because of this, the factor of  $i$  in Equation 3.18 has to be  $-i$  here, to ensure that there is no phase shift between the  $\mathcal{E}_z$  and the  $\mathcal{E}_x$  component in the far field, where the beam originates. Intuitively this can be seen, because the phase difference between the two components is proportional to  $-\arctan\left(\frac{z}{z_R}\right)$  and would therefore be  $\frac{\pi}{2}$  for the far field in negative z-direction without this compensating factor. Therefore, the combined longitudinal component of both beams will be:

$$E_z(\vec{r}) = \frac{2E_0}{z_R} \frac{x}{1 + \left(\frac{z}{z_R}\right)^2} \exp\left(-\frac{r^2}{w(z)^2} + i\omega t + i\frac{\Delta\varphi}{2} + i\pi\right) \cdot 2 \sin\left(kz + k\frac{r^2}{2R} - 2 \arctan\left(\frac{z}{z_R}\right) - \frac{\Delta\varphi}{2}\right), \quad (4.5)$$

where the factor of -1 was written as  $e^{i\pi}$  to make it obvious that the phase difference between  $E_z$  and  $E_x$  equals  $\pi$  everywhere compared to  $\arctan\left(\frac{z}{z_R}\right) + \frac{\pi}{2}$  for the RW (see section 3.2). Thus the elliptical polarization in the focus is completely eliminated, although the longitudinal components are still present. But as they now also have a spatial phase shift relative to the transversal components, they are minimal, in the centre of the pockets, where the atom will be. Mind that, the polarization vector will still point in different directions at different positions along the optical axis and even will point completely in longitudinal direction at the minima of the intensity, but the effective magnetic field will be zero everywhere.

### 4.3. The Effect of Misalignments

The calculations presented in the previous section were under the assumption of perfectly overlapped beams. In a real experiment this will not be the case. Therefore, the

effect of imperfect overlap of the two beams on the effective magnetic field has to be studied. In the following subsections all plots of the effective magnetic field are for a trap depth  $U_{0SW} = k_B \cdot 3.2\text{mK}$ . This value is chosen for good comparability with the current experimental setting, presented in section 3.3.2, but the trap can be operated with lower values as well, resulting in a linear decrease of the effective magnetic field. In the following contour-plots of the effective magnetic field, colorbar-scalings are kept constant for the different plots, to allow good comparability between the pictures.

The effective magnetic fields are calculated by evaluating the approximated expressions for the electric fields in x- and z-direction (equations 2.2 and 3.18) for both beams, in an individual coordinate system. The coordinate system of the first beam is as presented in Appendix A. The fields introduced by the second beam are calculated by applying a coordinate transformation on the first beam, depending on the misalignment parameters. Then the electric fields are added and the effective magnetic field is derived according to equation 3.20.

The effect of the misalignment on the geometry of the potential is taken into account in the shape of the ellipses, indicating the position of the atom, but will not be discussed in detail, as it is very small for the presented parameter ranges.

### 4.3.1. Transversal Displacement

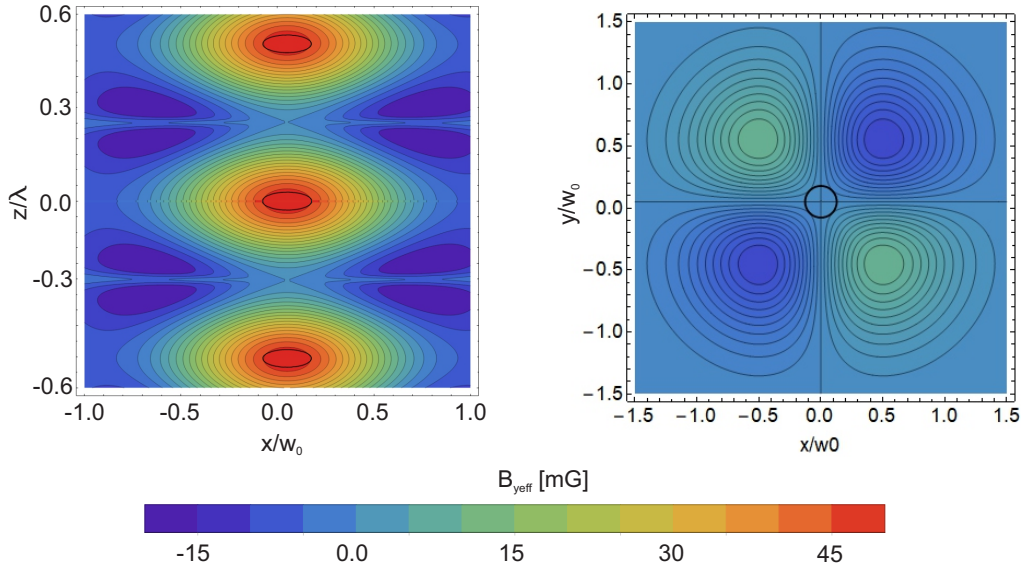


Figure 4.3.: The Effective magnetic field for  $\Delta x = 0.1w_0$  (left)  $\Delta y = 0.1w_0$  (right). Note that the left figure shows the xz-plane ( $y=0$ ) and right the xy-plane ( $z=0$ ). Black ellipses indicate the confinement area for atomic temperature  $T = 50\mu\text{K}$  with  $U_{0SW} = k_B \cdot 3.2\text{mK}$

The beams can be displaced transversally relative to each other. The resulting fields of such a misalignment are shown in figure 4.3.

## 4. Standing Wave Dipole Trap

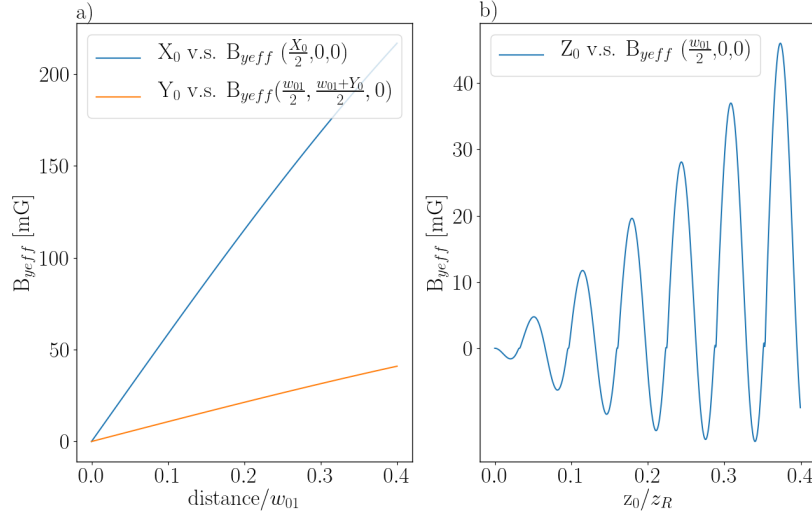


Figure 4.4.: Maximum effective magnetic field introduced by beam misalignment in x-, y- (a) and z-direction (b). The values increase linearly in (a). The oscillations in (b) occur due to the fact, that the values of  $B_{y,eff}$  are always taken at a constant position, while the structure in figure 4.5 is moving when  $Z_0$  is changing because the phase of the beams in the calculation programme is defined relative to their focus position. The small dips at the zero-crossing of the oscillations can be explained by the change in shape, that occurs for the outer lying maxima. However, the amplitude of the oscillations is growing linearly.

A displacement in y-direction ( $\Delta y$ ) only creates minimal fields, that additionally have a zero-crossing at the position of the atom. Therefore the differences the atom will see are minimal and are easily suppressed by a guiding field.

A displacement along the polarization axis ( $\Delta x$ ) will create large effective fields with a maximum at the position of the atom. But also these have a rather flat top, such that the differences in magnetic field, the atom will see, are not substantial. The magnetic field offset, can be cancelled on average by a magnetic compensation field along the y-axis. The field can be set accurately by minimizing the Larmor precession of the atomic state. The height of the maxima will slowly decay in z-direction, but only by 10% of the maximum value within the area where the atoms will be confined.

Up to a misalignment of  $0.4w_0$  the maximum effective field will increase approximately linearly for both misalignment parameters, see figure 4.4.

### 4.3.2. Longitudinal Displacement

If the foci of the beams are at different longitudinal positions with distance  $\Delta z$  this will cause alternating fields on both sides of the z-axis, as shown in figures 4.5 and 4.6. In this case, the atom can be in the regions of high gradient, but the maximum fluctuations

in magnetic field are only 15mG, what is still in the range that can be suppressed with a guiding field. As visible in figure 4.4 the fields will increase linearly, in  $z_0$ .

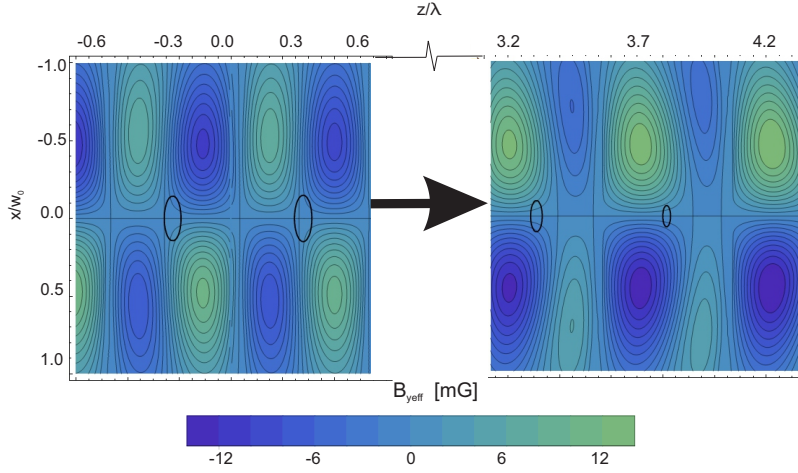


Figure 4.5.: Effective magnetic field for a misalignment of  $\Delta z = 0.1z_R$  in the  $y=0$  plane for  $U_0 = k_B \cdot 3.2$  mK. Black ellipses indicate the confinement area for atomic temperature  $T = 50\mu\text{K}$ .

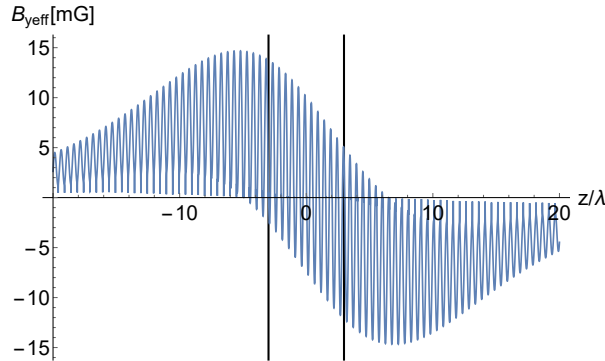


Figure 4.6.: Profile of effective magnetic field if  $\Delta z = 0.1z_R$ . Profile is taken along the line  $x=w_0/2, y=0$ . Black lines indicate  $\pm z_{max}$  as defined in equation 4.3 for  $U_0 = 3.2\mu\text{K}$ .

### 4.3.3. Angular Misalignment

An angle between the beams in  $x$ -direction ( $\alpha_x$ ), will result in a field distribution as shown in figure 4.7. Around the pockets in which the atom will be trapped, elliptical regions of effective magnetic field with alternating sign arise. These fields can exhibit a significant gradient in the region where the atom will be. Outside the focal plane the regions high of effective magnetic field will get deformed, moving the area of high field

#### 4. Standing Wave Dipole Trap

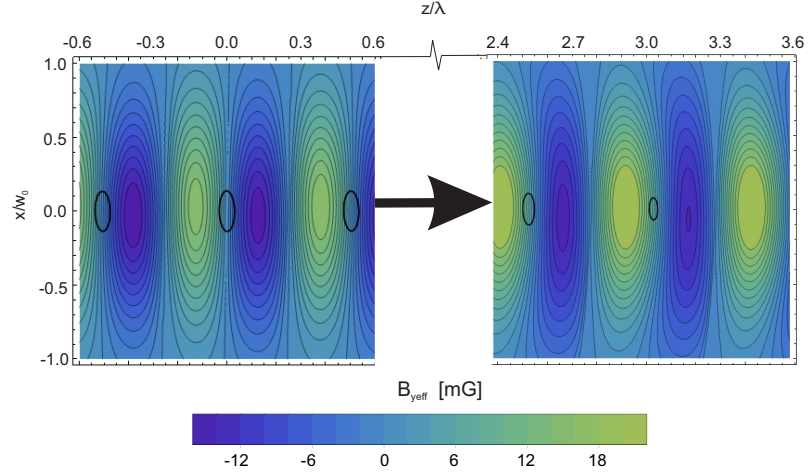


Figure 4.7.: Effective magnetic field for  $\alpha_x = 0.5^\circ$  around the focus (left) and around  $z_{max}$  (right) as defined in equation 4.3 for  $U_0 = k_B \cdot 3.2$  mK. Black ellipses indicate the confinement area for atomic temperature  $T = 50 \mu\text{K}$ .

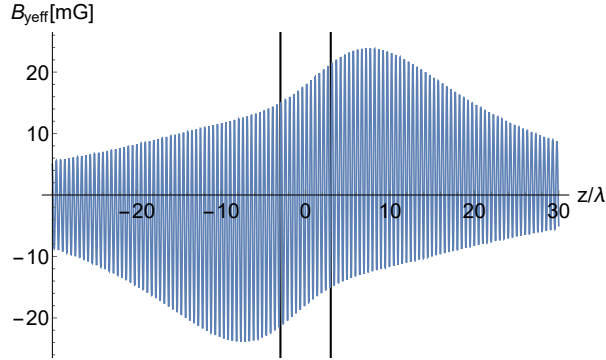


Figure 4.8.: Profile along the  $z$ -axis of effective magnetic field if  $\alpha_x = 0.5$ . Black lines indicate  $z_{max}$  as defined in equation 4.3 for  $U_0 = 3.2 \mu\text{K}$ .

closer to the atom. Additionally, the maximum values of the field, will increase outside the focus, before they decrease again (see figure 4.8).

A misalignment angle in  $y$ -direction ( $\alpha_y$ ) will cause fields, as sketched in figure 4.9. This image is taken in the  $z = z_{max}$  plane because the field amplitudes will decay towards the focus, as shown in figure 4.10. As shown, these effective fields are very low compared to misalignment along the polarization axis and the highest amplitudes lie outside the area the atom can reach.

The effective fields will increase linearly for both misalignment parameters (see figure 4.12).

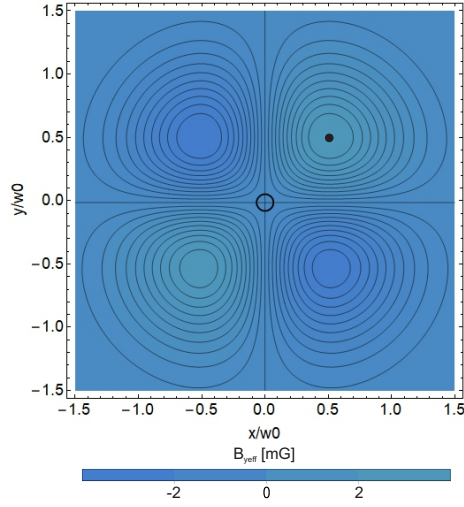


Figure 4.9.: Effective magnetic field if  $\alpha_y = 1.0$ , in the  $z = z_{max}$  plane, as defined in equation 4.3 for  $U_0 = k_B \cdot 3.2$  mK. Black ellipse indicates the area where 95% of all  $50\mu\text{K}$  atoms will be confined. Black spot shows the axis of the profile in figure 4.10

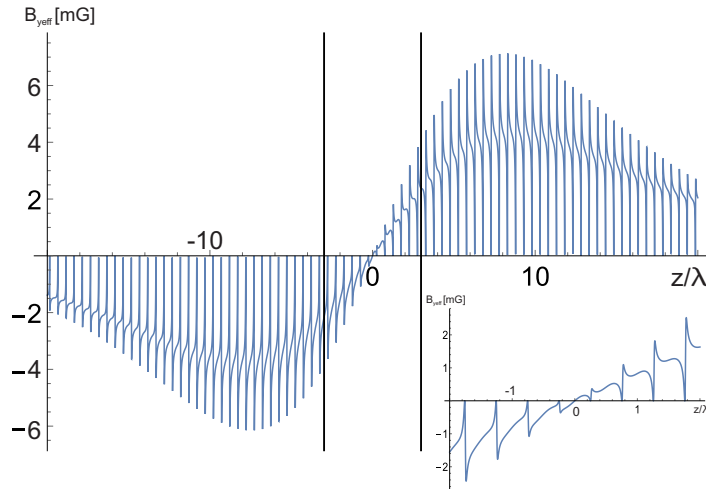


Figure 4.10.: Profile of effective magnetic field if  $\alpha_y = 1.0$ . Profile is taken along the line  $x=y=w_0/2$ , as shown in figure 4.9. Black lines indicate  $\pm z_{max}$  as defined in equation 4.3 for  $U_0 = 3.2\mu\text{K}$ . Inset shows zoomed in version around the focus. The atom will be trapped at positions  $z=0$  and integer multiples of  $z/\lambda = 1/2$ .

## 4. Standing Wave Dipole Trap

### 4.3.4. Different Focus Waists

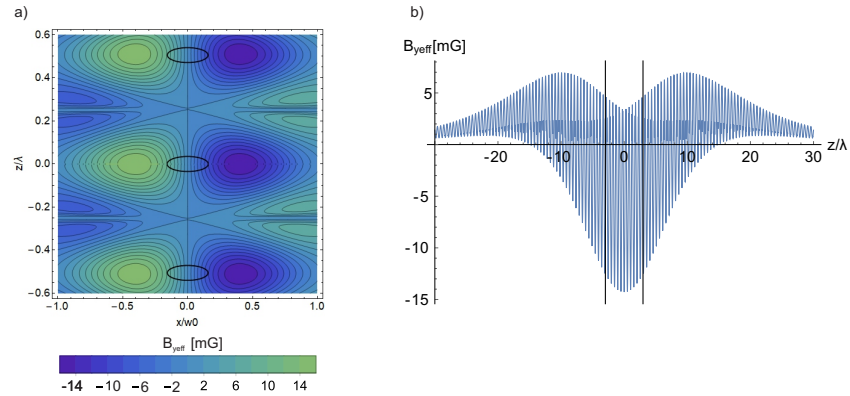


Figure 4.11.: Effective magnetic field if the the waists of the beams differ by  $\frac{w_{02}}{w_{01}} = 0.95$  for  $U_0 = k_B \cdot 3.2$  mK. (a): in the  $y=0$  plane; black ellipses indicate the confinement area for atomic temperature  $T = 50 \mu\text{K}$ . (b): Profile along the line  $y=0$ ,  $x=\frac{w_0}{2}$ . Black lines indicate  $\pm z_{max}$  as defined in equation 4.3

Also the focus size of the two beams can differ. This will lead to effective fields as shown in figure 4.11, with the atom seeing significant gradients in effective magnetic field, even for the small difference of just 5% of the waist. As visible in figure 4.12 the absolute height of the maxima, will increase linearly with the ratio  $\frac{w_{02}}{w_{01}}$ .

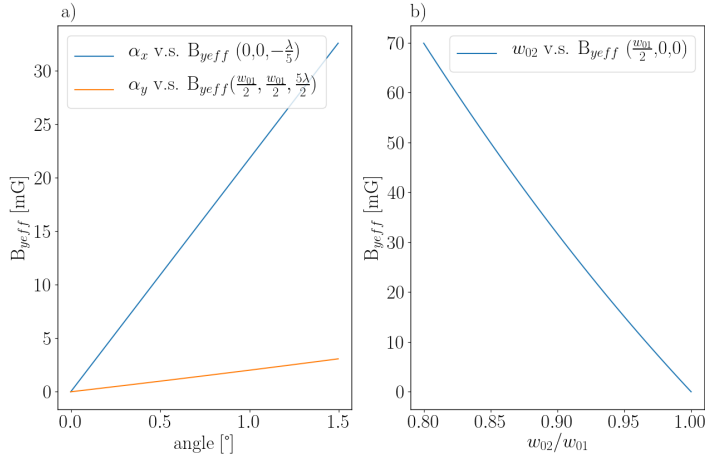


Figure 4.12.: Effective magnetic field approximately at the position of its maximum, plotted against misalignment parameters  $\alpha_x$  and  $\alpha_y$  (a) and  $\frac{w_{02}}{w_{01}}$  (b). The values increase linearly in a) and b) for growing misalignments.

#### 4.3.5. Different Intensities of the Beams

Finally, not only the geometric parameters of the beams can differ, but also their powers  $P_1$  and  $P_2$  can be unbalanced. The fields introduced by such a mismatch, are shown in figure 4.13. The maximum differences in these fields are well below 25 mG, even for the rather pessimistic choice of 10% difference in power. By a simple active stabilisation it should easily be possible to achieve better balance of the powers. As visible in figure 4.14, the maximum field amplitudes are also linear in the ratio of the beam powers and will thus be even lower in this case.

#### 4. Standing Wave Dipole Trap

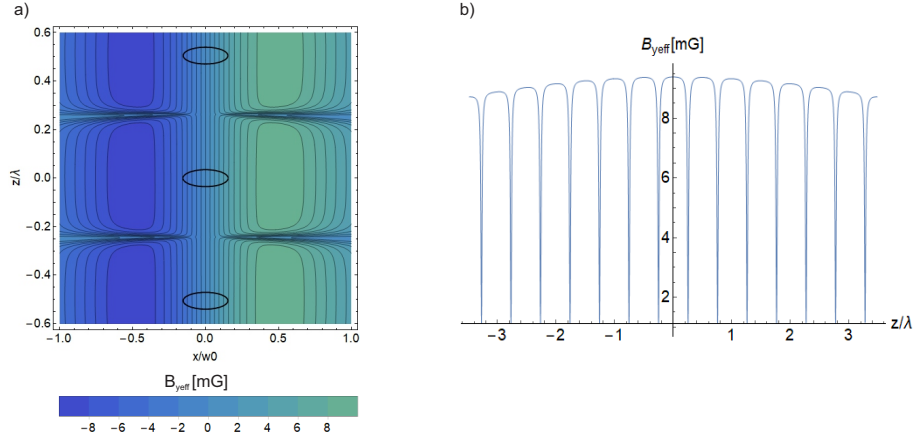


Figure 4.13.: Effective magnetic field if the the powers of the beams differ by  $\frac{P_2}{P_1} = 0.9$  for  $U_0 = k_B \cdot 3.2$  mK, in the  $y=0$  plane (a) and along the line  $y=0, x=\frac{w_0}{2}$  (b). Black ellipses indicate the confinement area for atomic temperature  $T = 50\mu\text{K}$

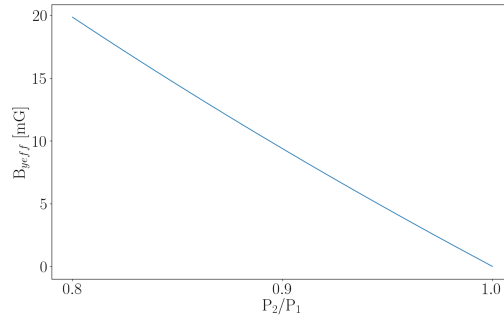


Figure 4.14.: Effective magnetic field approximately at the position of its maximum, plotted against the ratio of the beam powers.

#### 4.3.6. Summary

As shown in the previous sections, a relative displacement in x-direction (i.e. the polarization axis), an angle between the beams in x-direction and different waist sizes will cause the highest effective magnetic fields at the position of the atom.

The first effect can be cancelled with a compensating magnetic field in y-direction. The latter two will require a precise adjustment of the beam alignment and a guiding field to suppress residual effective magnetic field effects.

All other misalignments will, within reasonable boundaries, only create effective field fluctuations below 10mG around the position of the atom and can therefore easily be taken care of by a guiding field. All these fields will scale roughly linear with the misalignment parameter and the trap depth. Therefore, even if the misalignment is larger than assumed here, the fields can be reduced again, by decreasing the trap depth.

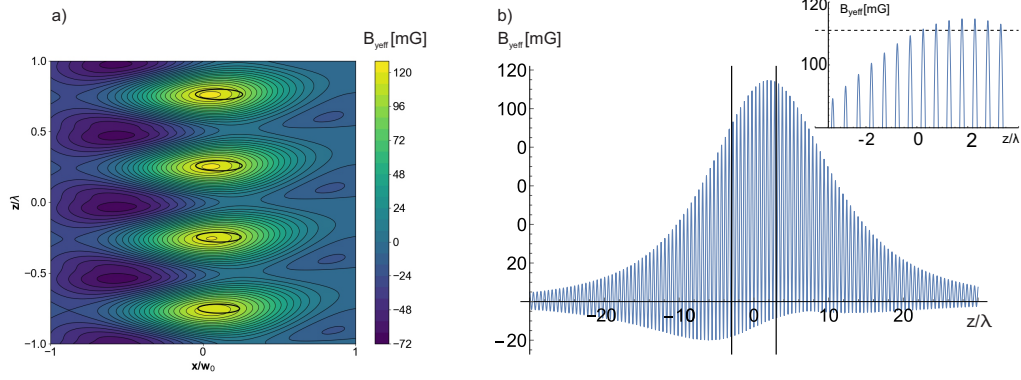


Figure 4.15.: Effective magnetic field with misalignments as given in table 4.1 a). Left: Contourplot in the  $y=0$  plane; Black ellipses indicates the area where 95% of all  $50\mu\text{K}$  atoms will be confined. Right: profile along the  $z$ -axis. Black lines indicate position of  $\pm z_{max}$ . Inset same parameters as b), zoomed in to  $\pm z_{max}$ . Horizontal line indicates amplitude of effective magnetic field in central pocket.

	$\Delta x$	$\Delta y$	$\Delta z$	$\alpha_x$	$\alpha_y$	$\frac{w_{02}}{w_{01}}$	$\frac{P_2}{P_1}$
a)	$0.2w_0$	$0.2w_0$	$0.1z_R$	$0.5^\circ$	$1.0^\circ$	0.9	0.9
b)	$0.1w_0$	$0.1w_0$	$0.1z_R$	$0.5^\circ$	$0.5^\circ$	0.95	1

Table 4.1.: Misalignment parameters chosen for an exemplary calculation.

The trap depth of  $k_B \cdot 3.2$  mK was chosen to reduce the rephasing time, however aiming for long distance entanglement, lower trap depths appear to be favourable. Executing a currently implemented experimental sequence with a trap depth of  $k_B \cdot 1$  mK should be possible.

Combining the misalignments creates an effective field distribution as shown in figure 4.15, which results in field differences the atom will see as shown in figure 4.16. The maximum fluctuations stay below 25mG, what a guiding field can suppress for atom temperatures up to  $60\mu\text{K}$ . So this regime can be reached without additional cooling periods as introduced in section 3.4.2). Interestingly, a small increment in the displacement in  $x$ -direction will even reduce the fluctuations, as then the maximum of the field will move closer to the pocket where the atom is trapped, exposing it to the flat top of the field distribution, instead of its slope.

Simulations of the resulting state evolution are shown in figure 4.17. With the misalignment parameters in table 4.1 a) and a trap depth of  $U_0 = k_B \cdot 3.2$  mK, it is not possible to meet the coherence requirements, but lowering the trap depth to  $U_0 = k_B \cdot 1.0$  mK already results in an almost ideal evolution. The long term evolution with these optimal parameters is shown in figure 4.18, suggesting coherence times up to 1.5 ms for the chosen configuration. All simulations are done with the atom in the central pocket.

#### 4. Standing Wave Dipole Trap

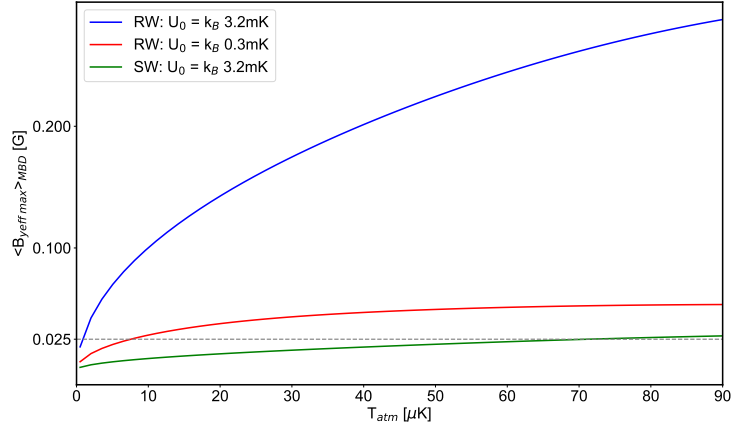


Figure 4.16.: Differences in  $B_{y,eff}$  the atom sees averaged over the MBD for different temperatures ( $T_{atm}$ ), as in figure 3.7 with the graph for a SW trap with misalignments as given in table 4.1 a) added. Standing wave trap average is done over all pockets visible in figure 4.15. The maximum difference the guiding field can suppress is 25mG (grey line).

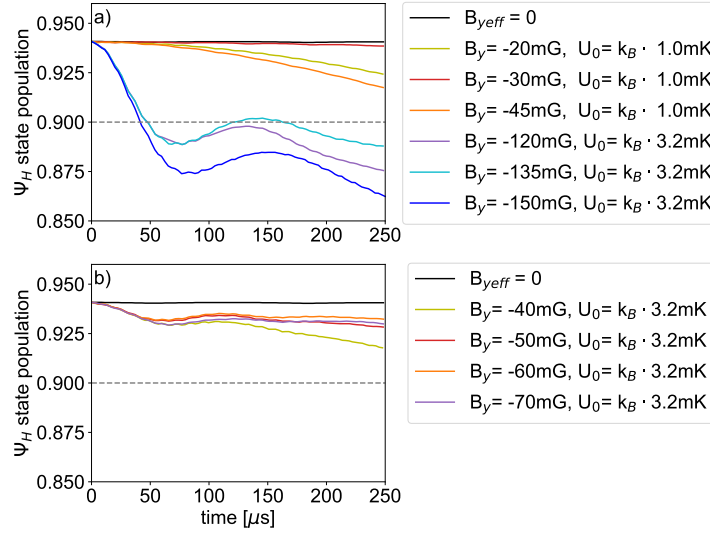


Figure 4.17.: Envelopes of the simulated evolutions of the state population in the dipole trap, if  $\psi_H$  is prepared, for different trap parameters. Misalignments as in table 4.1 a) (top) and b) (bottom). In a), one set with lower trap depth is added. Every parameter configuration, is run with three different compensation fields, showing that small errors in the strength of compensation field, will only have a limited effect. All evolutions are calculated with state transfer and  $B_z=250\text{mG}$  guiding field like in figure 3.9 c).

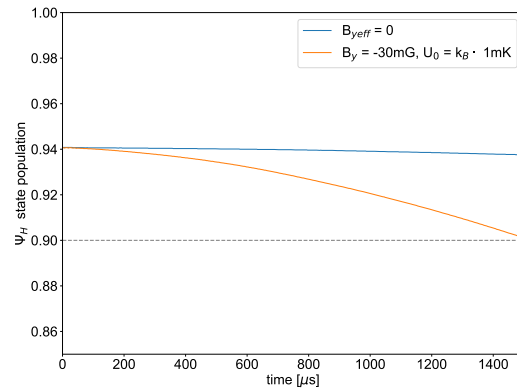


Figure 4.18.: Envelopes of the simulated evolutions of the state population in the dipole trap, if  $\psi_H$  is prepared, with trap parameters as in table 4.1 a) and optimum compensation field, for up to 1.5ms.

## 4.4. Loading the Atom in the Central Pockets

As visible from figure 4.15b), the offset in effective magnetic field can vary between different pockets, furthermore a higher  $\Delta z$  will increase this effect, as the focal plane will be further in the slope of the envelope. For the misalignment chosen in table 4.1 a), only trapping the atom reproducibly in one of the central three pockets, will reduce the differences in effective magnetic field to the values in figure 4.16.

The graphs in figure 4.17 suggest that the coherence time only weakly depends on the compensation field. Variations of  $\pm 5\%$  seem to have only a little influence. This suggests, that also such differences in the offset field, might have only little influence. Thus this criterion can also be reduced to the central 5 pockets.

Beside the reduced effective field fluctuations also the efficiency to collect photons and couple them into the fibre will be increased in the central pockets, compared to the outer ones.

As mentioned above, the atom first has to be trapped in the RW trap, to ensure loading of only a single atom. For the current maximum trap depth of  $k_B \cdot 3.2\text{mK}$   $z_{max}$  equals  $2.9\ \mu\text{m}$ . However, using readily available laser powers, trap depths up to  $k_B \cdot 16\ \text{mK}$  can be realised with a single beam. Resulting in stronger confinement and, reducing  $z_{max}$  to  $1.3\ \mu\text{m}$ . Hence shortly ramping up the RW trap, can load the atom most certainly into the central 7 pockets of the SW potential.

Using the harmonic approximation of the ODT-potential, the longitudinal thermal distribution of the atom within the trap is Gaussian with the width  $\sigma_L = \sqrt{\frac{k_B T}{m} \cdot \frac{1}{\hbar \omega_L}}$ , where  $\omega_L$  is the longitudinal trap frequency from equation 2.6 [16]. Therefore, the probability to find the atom in one of the three central pockets after turning on the second beam can be calculated as

$$P(p = \pm 1, 0) = \int_{-\frac{\lambda}{2}}^{\frac{\lambda}{2}} dz N \exp\left(-\frac{z^2}{2\sigma_L^2}\right) = \text{erf}\left(\frac{\lambda}{2z_R} \sqrt{\frac{U_0}{k_B T_{atm}}}\right) = 0.58, \quad (4.6)$$

where the pockets  $p$  haven been labelled by their number, along the  $z$ -axis, with 0 in the centre,  $N$  is a normalisation constant and  $\text{erf}()$  the error function.

So the atom will be in the central 3 pockets in 58 % of all cases. In these three pockets, the maximum effective magnetic fields are 120 mG - 125 mG. But in the other cases, the atom will be in the pockets  $p = \pm 2, \pm 3$ , seeing effective field differences of up to 20mG, allowing a less precise compensation field.

This section will explain how the position of the atom in the SW-trap can be determined and presents two suggestions how to prepare it in one of the central pockets.

$N_0$	$N_{\pm 1}$	$N_{\pm 2}$	$N_{\pm 3}$
214	211	202	189

Table 4.2.: Mean expected count rates  $N_{\pm p}$  if the atom is in pocket  $\pm p$ 

#### 4.4.1. Detecting the Position of the Atom

Currently, the fluorescence of the atom of the cooling lasers is used to detect, whether an atom is loaded into the ODT (see section 2.2.2). The fluorescence light is collected by the high-NA objective and coupled into a single mode fibre, guiding it to single photon detectors. The count rate of the detectors increases significantly, when an atom is loaded into the trap. The count rate is integrated over 40 ms to distinguish whether or not an atom is trapped.

When there is no atom in the trap, 18 counts are registered on average. They consists of dark counts of the APD and scattering of cooling light [40]. With an atom in the trap, this increases to around 200, depending on the detuning of the cooling lasers. Hence the counts produced by the atom are 182 on average.

The count rate also depends on the position of the atom in the trap, as this will influence the efficiency of the photon collection by the objective and the coupling into the fibre. The values given above, are the average over the thermal distribution of the atom in a RW trap. But in a SW trap, the atom will be localized in one pocket. Hence the number of fluorescence counts will be increased for the central pockets, as the mode overlap of the emission profile with the fibre mode will be better. On the other hand, it will be reduced in the outer lying pockets. This behaviour is also approximately symmetric around the central pocket.

Therefore, it is possible to determine whether the atom is in one of the central pockets, from the counts of the fluorescence measurement. For each pocket, the expected count rate is different, but all of them will follow a poisson distribution, given by:

$$P_p(k) = \frac{N_p^k e^{-N_p}}{k!}, \quad (4.7)$$

where  $p$  is the pocket index,  $N_p$  the expected number of counts from that pocket and  $k$  the number of registered counts in 40ms integration time. The expected mean number of counts for the different pockets in the current setup is given in table 4.2 and can be calculated by integrating the mode overlap of the atoms emission profile with the fibre mode. These numbers can also be tuned by adjusting the settings of the fibre coupler, e.g. optimizing them to be most sensitive for the central pocket. Calculations for these numbers and their dependency on the fibre coupler parameters can be found in [35]. The distributions up to the fourth pocket are shown in figure 4.19

In order to decide whether the atom is in the central pockets a value of the counts after 40ms integration time has to be chosen. Above this value one will assume that the atom is in the central pockets. This value should be so high, that the probability that

#### 4. Standing Wave Dipole Trap

the atom is actually not in the central pockets but in the next one in this case, is below 4%.

To prepare the atom reliably in the central three pockets, only events with more than  $N_{acc\pm 1}=228$  counts should be accepted, while for the central five pockets, events with  $N_{acc\pm 2}=213$  or more counts can be accepted. Both values are visualized by the black lines in figure 4.19.

The picture shows, that the probability to detect 228 counts is very low, even if the atom is in the central three pockets, as this value is higher than the mean values of the distributions of pockets 0 and  $\pm 1$ . Therefore, it will only be possible to localize the atom in the central 5 pockets.

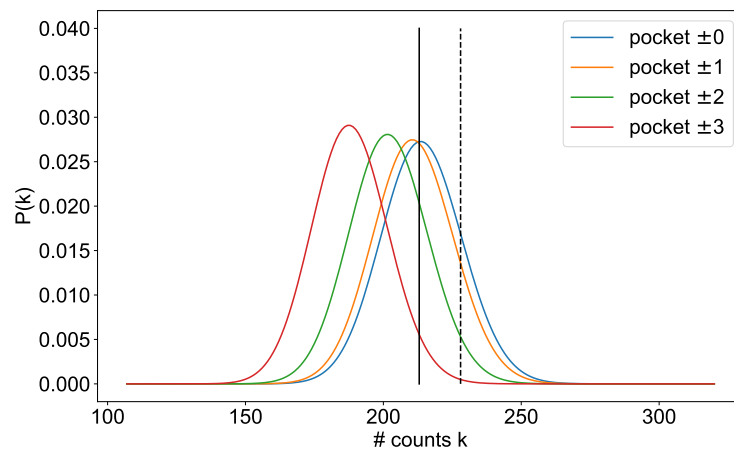


Figure 4.19.: Probability distributions of the fluorescence count rates, if the atom is in different pockets. Black lines show the necessary values to verify with more than 96% probability that the atom is in the central 3 (dashed) and the central 5 (solid) pockets .

#### 4.4.2. Moving the Atom to the Centre

As the atom will only be in the central three pockets in 58% of the cases, a method to prepare it there deterministically is needed.

One possibility to achieve this is to turn on the SW, and measuring the fluorescence. If the atom is found to be in the central pockets, the process is finished. If this is not the case, the SW can be turned off and on again, and the fluorescence can be remeasured. After a finite number of tries, the atom will be in one of the central pockets.

The probability for a successful preparation in the pockets with index up to  $p$  can be calculated as:

$$P_{success}(p) = \sum_{p'=0}^p P(p')P_{p'}(k > N_{acc\pm p'}), \quad (4.8)$$

where the probability to prepare the atom in pocket  $\pm p$ ,  $P(p)$  can be calculated by adjusting the boundaries of the integral in equation 4.6. The probability to get more than  $N_{acc\pm p}$  counts, if the atom is in pocket  $\pm p$ , can be derived from integrating equation 4.7.

This yields a success probability of 12% for the central three, and of 42% for the central five pockets. The probability that  $T$  tries are needed for a successful preparation can be calculated as:

$$P_{prep,p}(T) = P_{success}(p) \cdot (1 - P_{success}(p))^{T-1} \quad (4.9)$$

Thus for the central 5 pockets, on average 2.38 tries will be required for a successful preparation, but to prepare it in the central three pockets will require 8.69 tries on average. Every try will require at least 40ms for the fluorescence collection.

The exact count rates highly depend on different parameters of the experiment, like the detuning of the cooling light. Therefore, the exact numbers for the probabilities here might vary. But the general behaviour, that the central 3 pockets, are hard to distinguish from the central one, will stay the same.

Hence the process can also be improved, by increasing the number of scattered photons by temporarily decreasing the detuning of the cooling light. E.g. if  $N_0=500$ , the probability to successfully prepare and detect in the central three pockets becomes 20% for every try.

### Moving the Pocket with the Atom

Another option to prepare the atom in the central five pockets would be to move the pockets of the standing wave by a controlled phase shift. The problem of this method is that, it is not possible to determine from the fluorescence counts in which direction the atom has to be moved. Additionally, even when the atom is in the central five pockets, the probability to get more than 213 counts is only 47 %. Therefore, it can also easily happen that the atom will be moved, even when it is in the central five pockets.

For these two reasons a protocol employing this method will require on average more fluorescence collection intervals and hence take longer than the probabilistic method discussed above.

## 4.5. Trap Operation

Based on the findings in this chapter the following protocol to operate the SW trap is suggested:

- step 1: An atom is cooled and trapped in the RW potential of beam 1. This is necessary to make sure, only a single atom is loaded into the trap, which approximately takes 1s.
- step 2: Beam 1 is ramped up to maximum power, to confine the atom in the centre of the focus. All ramps have to be slow compared to the trap oscillation frequency, to ensure adiabaticity and thus avoid heating of the atom by the ramping procedure [16]. This results in a ramping time of approximately 0.1ms.
- step 3: Beam 2 is ramped up in roughly 0.1ms, trapping the atom in one of the pockets.
- step 4: The fluorescence is collected, to determine the position of the atom. If the counts are below 100, the atom was lost during the ramping process and one has to go back to step 1. If the counts are above 100, but below 213, an atom has been trapped, but is not in the central 5 pockets. Therefore, one has to ramp down Beam 2 and go back to step 3. If the number of counts is above 213, one can assume that the atom is in the central five pockets.
- step 5: The depth of the potential can be adapted to the requirements of the experiment. E.g. decreasing it slowly, will result in an even lower temperature of the atom, what might increase the coherence time. So the final adjustment of the potential depth will again take 0.1ms.

Altogether the average time required to load an atom can be calculated as:

$$t = 1s + 0.1ms + 2.38 \cdot (0.1ms + 40ms + 0.1ms) = 1095.776ms, \quad (4.10)$$

where the factor of 2.38 arises from the fact, that on average 2.38 tries will be required to load the atom in the central five pockets.

# 5. Experimental tests

In this chapter, several test setups implemented in this work to reach the requirements found in chapter 4 and results will be described.

As concluded in section 4.3 the spatial overlap of the two trapping beams has to be very good, i.e. all misalignment parameters from section 4.3 have to be minimized. Fibre to fibre coupling will be used to ensure good spatial overlap of the two beams. This overlap criterion will be verified by knife edge measurements of the two foci, described in section 5.1.

Secondly, the relative phase of the two beams has to be controlled precisely to ensure stability of the SW trap potential. Changes in the relative phase, will move the pockets of the SW potential and can heat the atom. Furthermore the atom has to be loaded into one of the central pockets reproducibly to reduce the effective field fluctuations the atom sees and enhance the photon collection efficiency. To achieve phase stability between the two beams, control of the phase of at least one beam is desired. The protocol to load the atom in one of the central pockets, derived in section 4.4, additionally requires control of the powers of both beams. A test setup to achieve these two controls employing acousto-optic modulators (AOMs) is presented in section 5.2.

## 5.1. Spatial Overlap

To couple a laser beam into a single mode fibre, good spatial overlap with the mode transmitted by the fibre is required. The coupling efficiency, defined as  $\eta = \frac{P_{in}}{P_{out}}$  where  $P_{in}$  and  $P_{out}$  are the power of the beam in the fibre and before the fibre, is directly proportional to the overlap integral of the electric fields of the fibre mode  $\mathcal{E}_{fib}(\vec{r})$  and the beam  $\mathcal{E}_B(\vec{r})$  :

$$|\langle \mathcal{E}_{fib} | \mathcal{E}_B \rangle|^2 = \left| \int d\vec{r} \mathcal{E}_{fib} \cdot \mathcal{E}_B^* \right|^2, \quad (5.1)$$

where  $\mathcal{E}^*$  stands for the complex conjugate of  $\mathcal{E}$  and the integral is over the mode area. For the  $TEM_{00}$  mode, both electric fields can be approximated by a Gaussian beam field distribution as described in equation 2.2. The fibre mode also defines the field distribution of a beam transmitted by the fibre. Therefore, the coupling efficiency of light emitted from one fibre and coupled into another can be used as an overlap criterion for the beams.

## 5. Experimental tests

Hence, the coupling efficiency is a precise measure for the spatial overlap close the the fibre couplers, but to verify, whether this criterion is sensitive enough to ensure perfect overlap of two micrometer-sized foci, an experimental setup was developed and implemented in the scope of this work. It will be described and analysed in this section.

### 5.1.1. Setup

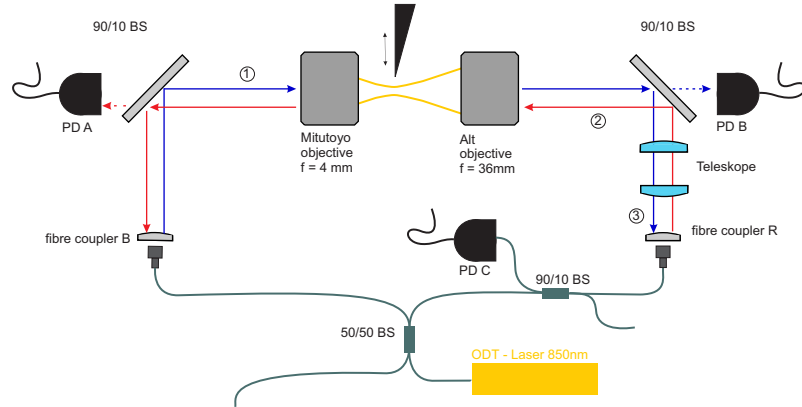


Figure 5.1.: Setup for measuring the overlap of two beams, depending on the coupling efficiency. Numbers in circles indicate positions where beam profiles in figure 5.2 were taken. Light beams are schematically shown offset from actual position for clarity.

A schematic of the experimental setup is shown in figure 5.1. Light from a 850nm diode laser is split into two beams by a 50/50 fibre BS. One beam (labeled blue (B)) is coupled out of the fibre with a waist of 0.56mm and focussed by a high NA objective<sup>1</sup> with a focal length of  $f_M=4\text{mm}$  and a working distance of  $d_w = 14\text{mm}$  to approximately  $3\ \mu\text{m}$  waist size. Behind the focus, the beam is collimated again by another high-NA objective using the design by Alt, presented in [2]. It has a focal length of  $f_A=36\text{mm}$ .

After recollimation, the beam is split by a 90/10 BS, of which the transmitted 10% part is focussed onto a photodiode (PD B). The reflected beam, is reduced by a 2:1 telescope, consisting of two one inch lenses in cage optics, with focal lengths  $f_1=60\text{mm}$  and  $f_2=30\text{mm}$ . Finally it is coupled into a fibre again, with the coupler red (R). After the fibre coupler, 10% of the light are coupled out with a fibre BS and guided to PD C. This signal is used to measure the power coupled back into the fibre.

The second beam (labeled red (R)) shares the same beampath, but counter-propagating. It is enlarged by the telescope and partly focussed on a photodiode (PD A) after passing through the two objectives.

<sup>1</sup>Mitutoyo, G Plan Apo 50, NA=0.5, corrected for a glass plate with a thickness of 3.5 mm between the objective and the focal spot.

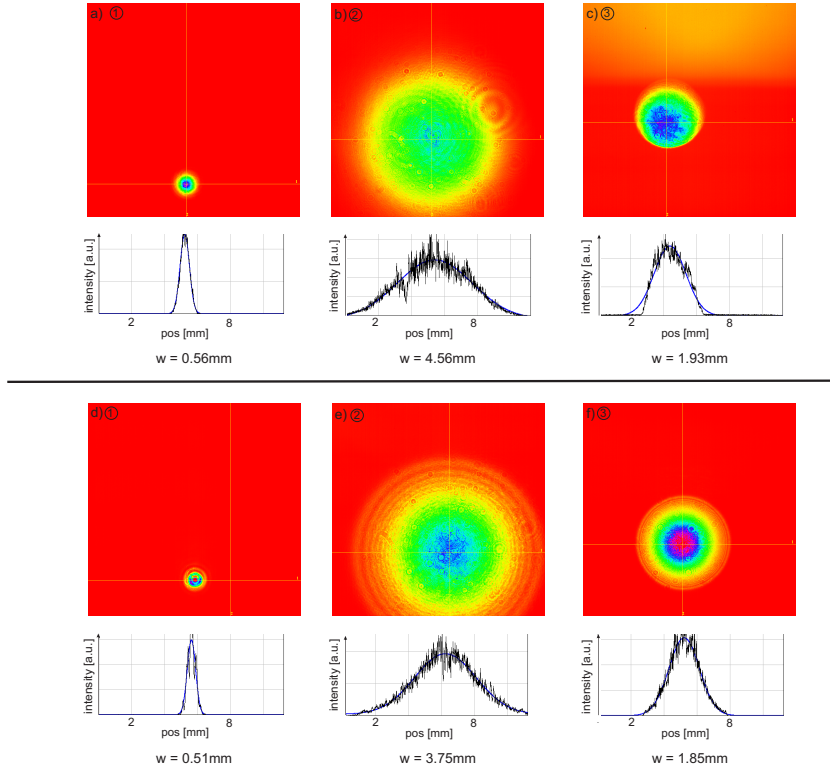


Figure 5.2.: Transversal intensity distributions of the B beam (top row) and R Beam (bottom row) numbers in circles, correspond to positions shown in figure 5.1 where the profiles were taken; together with intensity profiles in x-direction (black) and Gaussian fits (blue) to find the waist of the beam at that position. In (c) & (d) the deviation introduced by the telescope is clearly visible.

The telescope is required, to account for the different focus sizes of the beams, introduced by the different working distances of the objectives. Note that the extra optical components will introduce additional aberrations, causing deviations from a Gaussian beam profile. Resulting profiles of both beams before and after passing through the two objectives are shown in figure 5.2.

To characterize the beam profiles around the focus positions knife edge measurements are performed. Two sharp razor knives are mounted on a three dimensional stage driven by step motors with around 10nm precision. These can be moved into the beams from two directions (x and y), blocking them partly and therefore reducing the power on photodiodes PD A and PD B. The mounted knives are shown in figure 5.3. Intensities on the two photodiodes are recorded together with the position of the knife. By fitting the integrated intensity distribution of a Gaussian beam to the measured intensities, and positions of the knife edge, the waist at the position of the knife can be derived. By doing this scan once in x-direction and once in y-direction, the waist of the beam in

## 5. Experimental tests

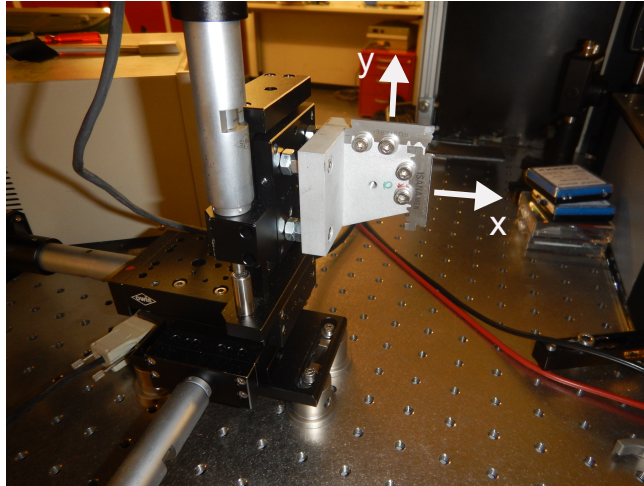


Figure 5.3.: The beam profile characterization setup, consisting of two razor blades, to perform knife edge measurements in two dimensions. Arrows indicate coordinate system.

both directions can be measured. By moving the knife edge along the beam, waists at different  $z$ -positions can be taken. From these, the minimal waist  $w_0$  of the beam can be derived again by fitting a Gaussian longitudinal intensity profile to these.

### Alignment

To achieve high coupling efficiency, precise alignment of all optical elements is crucial. Both objectives and lenses have to be hit central and perpendicular in order to minimize aberrations, causing deviations from the Gaussian beam field distribution and reducing the overlap with the ideal fibre modes.

To achieve this, fibre coupling is used as an alignment parameter for every single element. The following alignment procedure is used:

- step 1: A mirror and an iris are mounted on the side of the Mitutoyo objective pointing towards the B coupler and the reflection of the B beam is aligned such that it would hit the iris central and be coupled back into the fibre, observing the coupling efficiency at the free output of the 50/50 BS.
- step 2: The mirror and the iris are mounted on the Alt-Objective, which itself is mounted on a three axis translational- and a tip and tilt-stage. With these degrees of freedom, the Alt Objective is positioned and oriented such, that the B beam is again coupled back into the fibre. Both objectives mounted are shown in figure 5.4.

- step 3: The beam is collimated behind the Alt-objective by moving that along the beam axis. This is verified by recording the beam profile at different positions behind the objective with a CCD camera and positioning the objective such, that the waist is the same at different z-positions. One of the beam profiles is shown in figure 5.2 (b).
- step 4: The telescope is positioned by the same method relative to the B beam: an iris is installed in front of it and a mirror on the back. Back-coupling to the initial fibre through all the elements, is optimized.
- step 5: The red coupler is aligned by optimizing the power on PD C.

This alignment procedure ensures that the beams propagate through the centre of all elements, minimizing spherical aberrations. They will however still occur, due to the large beam diameters at some positions.

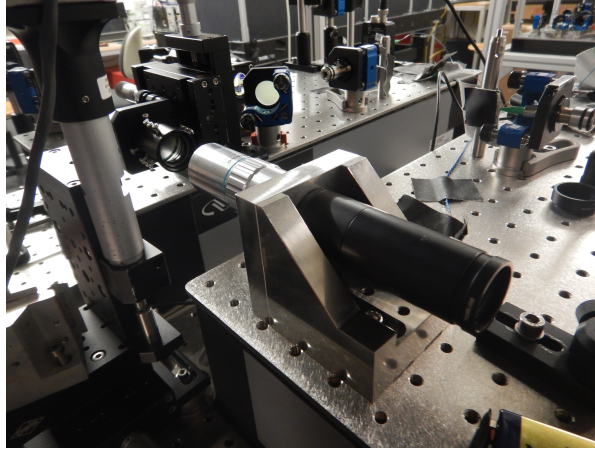


Figure 5.4.: Picture of the two objectives, Mitutoyo (silver) with the mounted mirror and iris in tube optics; Alt objective in the background (black).

### 5.1.2. Measurement Procedure

To eliminate backreflections from the knife edges and the objectives caused by the not measured beam, shutters are introduced in both beams, blocking each beam in front of its out-coupler while measuring the other one.

The following measurement protocol is used:

First the knife edge is moved completely into the beam in x-direction, at a z-position 0.2mm away from the focus. Then it moves out of the beam, in steps of 3  $\mu\text{m}$ . After every step, first the R-beam is blocked, while the B-beams intensity is recorded on PD B. Then the B-beam is blocked, recording the R-beam on PD A. While the knife edge is moving, both blockers are opened again.

After this x-scan a y-scan with the same parameters is done. This procedure is repeated at all z-positions visible in figure 5.5.

## 5. Experimental tests

The coupling efficiency is measured by comparing the values of PD B and PD C. Here the coupling efficiency is defined as the power just before the coupler R divided by the power, coupled into the fibre. Therefore, a correction factor F has to be used to derive the coupling efficiency from the measured power at the positions of the photodiodes. This factor is the power in front of coupler R divided by the power at the position of PD B. With these, the coupling efficiency is calculated as:

$$\eta = \frac{10 \cdot P_C}{F \cdot P_B}, \quad (5.2)$$

with the powers at the photodiodes  $P_B$  and  $P_C$ , correspondingly, taken at a position, where the knife has moved out of the beam entirely. The factor of 10 arises because PD C is installed at the 10% port of a 90/10 fibre BS. The value of  $\eta$  is taken at every z-position and averaged. The highest achievable coupling efficiency was 59% with a standard deviation of 1%.

To characterize the precision of the alignment criterion, the z-scan was repeated for 12 different coupling efficiencies, all achieved by intended misalignment in x-direction, by tilting the BS in front of PD B.

### 5.1.3. Evaluation of the Results

The expected power on the photodiodes for different transversal positions of the knife edge can be calculated by integrating a Gaussian intensity distribution over the area, not covered by the knife:

$$\begin{aligned} P(x) &= \int_{-\infty}^{\infty} dy \int_{-\infty}^x dx' \frac{4P_0}{\pi w_x(z) w_y(z)} \exp\left(-\frac{2(x' - x_0)^2}{w_x(z)^2} - \frac{2(y - y_0)^2}{w_y(z)^2}\right) \\ &= P_0 \cdot \operatorname{erf}\left(\frac{\sqrt{2}(x - x_0)}{w_x(z)}\right), \end{aligned} \quad (5.3)$$

x and y being the coordinates of the transversal plane and z pointing along the beam axis towards the Mitutoyo objective, a normalization constant  $P_0$ , the position of the knife edge x, the position of the beam axis ( $x_0$ ,  $y_0$ ), different local waists of the beam in x- and y-direction  $w_x(z)$  and  $w_y(z)$  as defined for equation 2.2 and the error function  $\operatorname{erf}()$ . Different waists in x- and y-direction are required because most real beams will not be rotationally symmetric like the ideal field distribution presented in equation 2.2, because of imperfections of the optical elements in the path.

After every x- and every y-scan  $x_0$  and  $w_x(z)$  or  $y_0$  and  $w_y(z)$  for both beams are found from fitting the above function  $P(x)$  to the measured distribution.

Later, the beam axes are found, by applying a linear fit  $ax(z) = m \cdot z + t$ , with parameters m and t to the  $x_0$  and  $y_0$  values of both beams. Also, a Gaussian waist

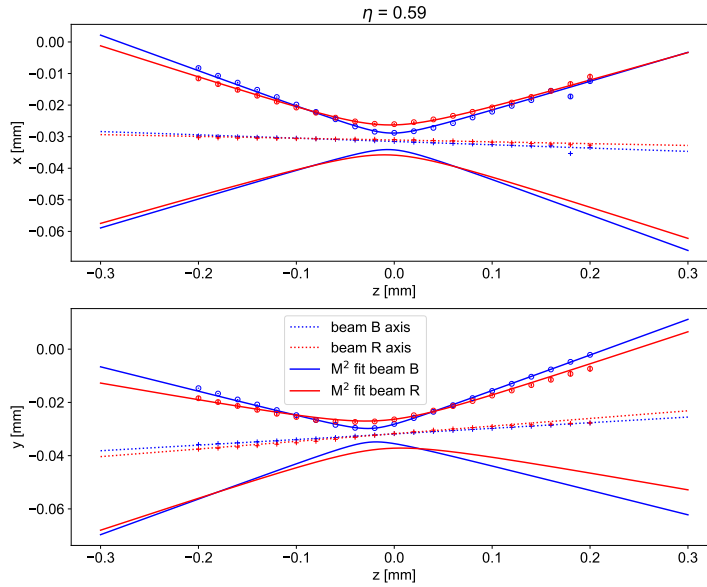


Figure 5.5.:  $M^2$  fits, beam axis and measured positions (crosses) and waists (circles) of both beams, in x- and y-direction. Fitted waists are  $w_{0xB} = 2.6\mu m$ ,  $w_{0xR} = 4.7\mu m$ ,  $w_{0yB} = 2.6\mu m$ ,  $w_{0yR} = 5.3\mu m$ . Errorbars are uncertainties of the erf-fits.

dependence is fitted to the found local waists for both beams, in x- and y-direction. According to the following function:

$$w(z) = w_0 \sqrt{1 + \left( \frac{M(z - z_0)\lambda}{\pi w_0} \right)^2}, \quad (5.4)$$

where the minimum waist  $w_0$ , its position along the z-axis  $z_0$ , and  $M$  are fit parameters. By adding the additional degree of freedom  $M$ , it is possible to find beam divergences, different from the expected value for a Gaussian beam with waist  $w_0$  [4]. Fitted function and measurement results with maximum coupling efficiency are shown in figure 5.5. All fit parameters are summarized in tables D.1 and D.2.

To illustrate the transversal positions of the beams relative to each other, ellipses with the corresponding beam waists as axes are drawn in figure 5.6.

Finally, the temperature stability of the entire setup was analysed. For this, the air temperature close to the table and the coupling efficiency were monitored for 39 hours. During this time, the knife edge measurements were also running, in order to identify movement of the beams. Results for all 3 parameters are shown in figure 5.7. Both, the coupling efficiency and the beam centre distance show a strong dependency

## 5. Experimental tests

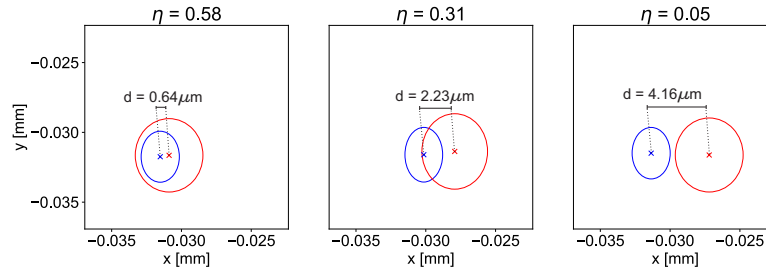


Figure 5.6.: Ellipses with corresponding beam waists as axes, at beam positions in the focal plane for 3 different coupling efficiencies. The beam centre distances  $d$  are calculated from the misplacements of the beams in x- and y- direction.

on the air temperature. Fluctuations of 0.5K can reduce the coupling efficiency by more than a factor of 2, but these fluctuations occur on a time scale much slower than one experimental run. After implementing the standing wave into the atom trap setup, air temperature fluctuations are reduced by active stabilization to 0.1K. Additionally, the beam paths will be significantly shorter, to reduce the temperature dependency. If these two effects turn out to be not sufficient, to minimize the fluctuations to below 10%, active pointing stabilization is required.

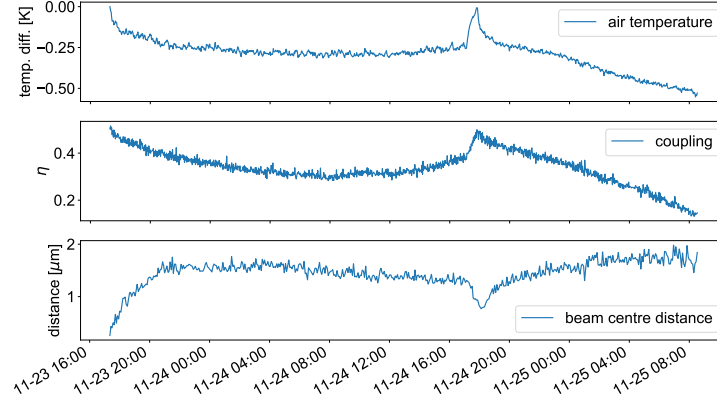


Figure 5.7.: Air temperature variations, Coupling efficiency and beam centre distance as shown in figure 5.6, monitored for 39 hours.

### 5.1.4. Discussion

The measured minimal waists of the R-beam are much larger than the ones of the B-beam. This might be due to deviations from the ideal Gaussian behaviour of the

R-beam, possibly originating from the telescope. This can also be seen by comparing the fit values of  $M$ , shown in figure 5.8: For the fits to beam B,  $M$  is roughly around one, indicating nearly ideal Gaussian behaviour, while from beam R, the values of  $M$  are around 1.8. Therefore the divergence of beam R seems to be much larger than expected for a Gaussian beam. These deviations from the  $\text{TEM}_{00}$ -mode, can also be the reason for the low achievable coupling efficiency.

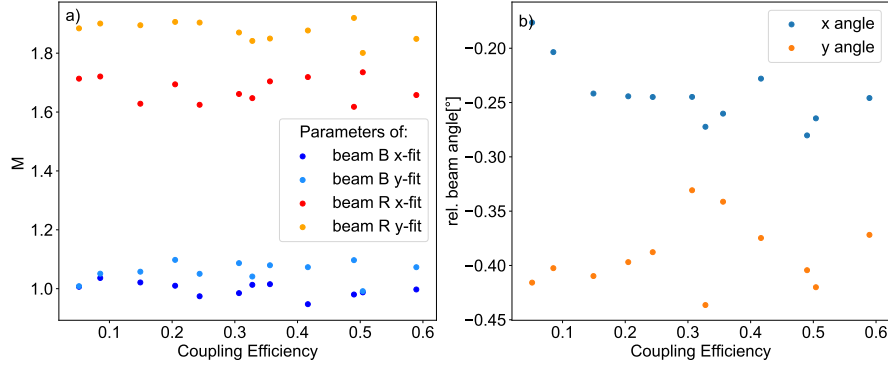


Figure 5.8.: a):  $M$  from the fits with different coupling efficiencies. b): relative angle of the two beams in both transversal directions.

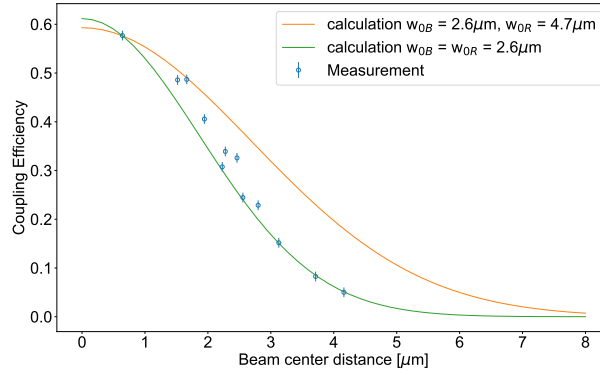


Figure 5.9.: Numerical evaluations of the overlap integral from equation 5.5 for different beam centre distances, with two combinations of waist sizes and the beam centre distances derived from the fits. Errorbars correspond to the 1% standard deviation coupling efficiency measurements. Evaluated curves are rescaled to fit with highest measured value

Interestingly, the misalignment, introduced by tilting the 90/10 BS closer to PD B, does not affect the angle between the beams, but only the positions of the beam axes. In figure 5.8 b) the angle between the beams in both directions are plotted against the coupling efficiency. They vary significantly, but if this was caused by the misalignment

## 5. Experimental tests

$\Delta x$	$\Delta y$	$\Delta z$	$\alpha_x$	$\alpha_y$	$\frac{w_{02}}{w_{01}}$
$0.25w_0$	$0.25w_0$	$0.25z_R$	$0.4^\circ$	$0.4^\circ$	-

Table 5.1.: Misalignment parameters derived from the measurement with  $\eta=59\%$ .

the x angle would have to increase constantly for lower coupling efficiencies. This is not the case, so the variations are rather caused by thermal movements of the measurement setup.

An expected coupling efficiency can also be calculated by evaluating the overlap integral of the electric fields  $\vec{\mathcal{E}}_B$  and  $\vec{\mathcal{E}}_R$ , of the two beams:

$$\left| \langle \vec{\mathcal{E}}_B | \vec{\mathcal{E}}_R \rangle \right|^2 = \left| \int d\vec{r} \vec{\mathcal{E}}_B \cdot \vec{\mathcal{E}}_R^* \right|^2, \quad (5.5)$$

with the integral running over the entire space and  $\vec{\mathcal{E}}_R^*$  being the complex conjugate of  $\vec{\mathcal{E}}_R$ . As the coupling efficiency into the fibre does not depend on the polarization of the beam, both electric field vectors can be treated as scalars. By assuming Gaussian field distributions in both beams this integral can be evaluated numerically for different parameters.

Figure 5.9 shows two curves of the expected coupling efficiency against the beam centre distance and the results of the knife edge measurements. The curves are calculated with different waists in x- and y-direction, but for the sake of readability, only the x-waists are given in the legend. Both curves are rescaled by a constant factor, to fit with the first measurement point. This is justified by the idea, that this factor quantifies the fraction of the R-beam, that has no overlap with the Gaussian mode any more. This fraction is lost for the fibre coupling, but the rest is still overlapping with the unperturbed beam and shows the expected dependence on the beam centre distance. This explanation is supported by the fact, that the green curve fits much better to the data than the orange one.

As the perturbed beam is the one that propagated through the telescope, the deviations are probably introduced by the latter. Therefore a future setup with identical objectives and without the telescope is planned.

From the presented results, values for the misalignment parameters discussed in section 4.3 can be derived. The values are shown in table 5.1. For  $\Delta x$  and  $\Delta y$  the distance of the beams is used, together with the waist of the B-beam.  $\Delta z$  is the average of the x and y scan. For  $\alpha_x$  and  $\alpha_y$  the larger relative beam angle is taken.  $\frac{w_{02}}{w_{01}}$  can not be derived from these measurements, as  $w_{0R}$  is not really known.

All these values are chosen rather pessimistic. They are also expected to become significantly smaller when two identical objectives are used and higher coupling efficiencies are reached. But they are already close to the exemplary values chosen for the simulations in section 4.3.6, for which successful enhancement of the coherence time can be

achieved.

## 5.2. Phase Stability

Thermal fluctuations and acoustic vibrations in optical components causing small deviations in the optical paths of the two beams will result in variations in the relative phase of the two SW-trap beams. Therefore, an active stabilization of the relative phase is necessary.

The relative phase of two beams can be measured by overlapping them on the active area of a photodiode, for example as shown in figure 5.11 and recording the PD signal. A right handed coordinate systems is used, with the centre of the PD at the origin. As usually, the z-axis is pointing in propagation direction of the beams, the x-axis is parallel to the optical table and the y-axis perpendicular to it, pointing upwards. The expected signal on the PD, is the spatial intensity distribution of two overlapped beams propagating in the same direction, integrated over the transversal plane, and evaluated at the z-position of the PD. The choice  $z=0$  in the plane of the photodiode, simplifies the expected power on the photodiode in case of perfect overlap to:

$$\begin{aligned} P_{PD}(t) &= P_0 \cdot \cos^2\left(\frac{\Delta\varphi(t)}{2}\right) \\ &= \frac{P_0}{2} \cdot (1 + \cos(\Delta\varphi)), \end{aligned} \tag{5.6}$$

where  $\Delta\varphi(t)$  is the phase difference between the two beams and  $P_0$  the added power of both. To avoid heating of the atom by movements of the trap, during an experimental procedure, it should be constant for the duration multiple excitation attempts. Here the requirement 0.1ms will be used.

An acousto-optic modulator can be used to shift the frequency of light by up to 200 MHz and can switch the the power within 20ns. It consists of a crystal, which is actuated by a piezo-crystal. Driving this piezo with a periodic signal, causes a running acoustic wave in the crystal. This will introduce a periodic modulation of the refractive index of the crystal, effectively producing a moving lattice for the laser beam, from which it is diffracted. Because of the movement of the lattice, the different orders of the diffraction pattern, are shifted in frequency. The  $\pm n^{th}$  order is shifted by  $\pm n$  times the driving frequency, with the positive orders beeing diffracted in direction of the lattice movement, hence away from the piezo introducing the acoustic waves. For efficient transmission usually only the first orders are used. To achieve the best possible performance with an AOM the beam is focussed into the optical crystal and collimated again afterwards. By varying the power of the driving signal the transmission of the AOM is controlled.

An AOM allows to control the power and phase of a laser beam. Therefore, a setup to test whether the phase can be stabilized by AOMs was designed. It will be presented

## 5. Experimental tests

in this section together with the obtained results.

### 5.2.1. Setup

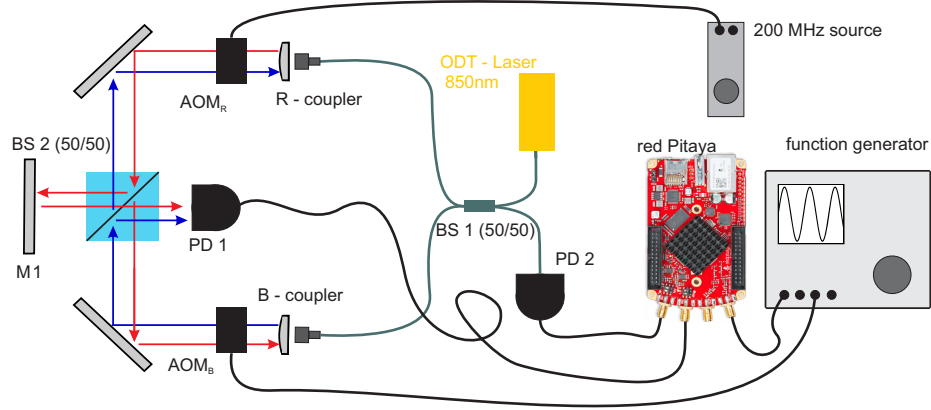


Figure 5.10.: Phase stabilisation setup. Lenses around the AOMs are not shown for reasons of clarity.

The setup is shown in figure 5.10. The beam from the ODT laser is split in two beams by a fibre beamsplitter (BS 1) and coupled out of the fibre. Both beams pass through an AOM, increasing their frequency by 200 MHz. The AOM at the red (R) beams coupler is driven by a constant source. The driving frequency of the AOM at the blue (B) beams coupler, is tuned by an active stabilization mechanism. This AOM will be called the controlled AOM in the following.

Then, 50% of both beam powers are coupled out of the path by the beamsplitter BS 2, reflected at mirror M1, and overlapped on a Photodiode (PD 1), as shown in figure 5.10. Mind that in the shown configuration only 25% of the (R) beam are reaching the PD, reducing the achievable contrast of the interference signal. This can be accounted for, by reducing the power of the B beam by the AOM<sub>B</sub>.

The rest of the beams will each pass through the AOM of the other beam, thereby again get the frequency shifted by the driving frequency and coupled into the fibre again. At BS 1, both are overlapped and guided on another photodiode (PD 2).

To ensure good spatial overlap at the position of BS 2, the fibre to fibre coupling was optimized before putting in BS 2. When adding BS 2, its orientation was aligned such, that it did not affect the fibre coupling efficiency. This was also required to enable good spatial and directional overlap of the Beams on PD 1, which is essential for good interference contrast.

The phase stabilization was done by a digital proportional-integral-derivative (PID) unit, running on a RedPitaya. A RedPitaya is a multi-functional electronic measurement device, based on a field programmable gate array (FPGA). It can be used as an

oscilloscope, function generator and spectrum analyser, up to frequencies of 50MHz. It provides two input and two output channels. Thanks to its python interface, it is also easily possible to adapt it to different requirements. In this work, the pid unit, from the python package pyrpl was used [28].

The signal from the two PDs are read out by the RedPitaya, while the RedPitaya also controlled the driving frequency of the controlled AOM via a remotely controllable function generator. The function generator was set such, that it would change the frequency of the driving signal, depending on the voltage output of the RedPitaya. Like this, the driving frequency could be set to defined values or be used as output of the PID unit.

If the frequencies of the beams differ by  $\Delta f$ , their interference signal at PD 1 will vary from minimum to maximum within  $t = \frac{1}{2\Delta f}$ . Therefore, to stabilize the beams for several ten milliseconds, their frequency difference must be smaller than 10Hz. Hence the 200MHz driving signal of the controlled AOM has to be adjusted, with a precision of 10Hz. If this precision is not reached, the pockets of the SW will always move. Therefore, a high quality function generator had to be used for this test setup, limiting the applicability of this method for the experiment.

### 5.2.2. Analysis of the Setup

The power measured by PD 1 will depend on the phase difference between the beams at the position of the PD  $\Delta\varphi_{PD1}$  (see equation 5.6). It is connected to the phase difference at the position of BS 2  $\Delta\varphi_{BS1}$  via:

$$\Delta\varphi_{PD1} = \Delta\varphi_{BS1} + 2kl + \frac{\pi}{2}, \quad (5.7)$$

with the distance between BS 2 and the mirror M 1. The phase difference of  $\frac{\pi}{2}$  is obtained from the different number of reflections each beam undergoes [1] and the propagation of the R-beam from the BS to the mirror and back. The propagation from BS 2 to PD 1 does not introduce a phase difference, as it is the same optical path for both beams. Figure 5.11 illustrates the acquisition of the phase difference.

Therefore, if the distance  $l$  is sufficiently stable, the phase difference at the position of PD 1 is directly related to the phase difference of the two counter-propagating beams. If the latter is varying over time, also the signal on PD 1 will vary, e.g. if the AOMs are driven at frequencies that differ by  $\Delta f$ :

$$\Delta\varphi_{BS1}(t) = 2\pi t\Delta f, \quad (5.8)$$

hence the signal on PD 1 will oscillate at the frequency difference of the two beams.

The signal of PD 2 will have a very similar dependence on the phase difference of the

## 5. Experimental tests

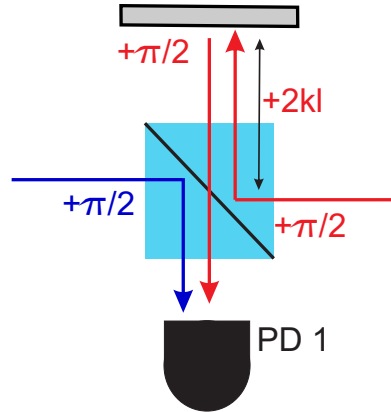


Figure 5.11.: Illustration of the phases obtained by both beams before hitting PD 1.

beams at the position of BS 1. But as both beams in such a Sagnac-configuration will have travelled along the exact same optical path at that position, this phase difference will be intrinsically stable. Therefore PD 2 is expected to give a constant signal, even when the AOMs are driven at different frequencies, as both beams will pass through both AOMs.

### 5.2.3. Measurements

The signal on both PDs was recorded with different settings for the controlled AOM.

Firstly, the driving frequency was set constant to 200 MHz. This yielded the signal shown in figure 5.12 (a): the interference signal on both PDs is oscillating at a varying frequency. This is probably due to imperfections in the uncontrolled AOM driver, which is not producing a perfectly constant frequency. Hence the frequency difference between the beams is varying, causing the oscillations in the interference signal.

Secondly, to verify the control over the interference signal, the frequency of the controlled AOM was varied in a triangle shape. It was varying by  $\pm 38\text{kHz}$  from the set 200 MHz of the other AOM, with a period of 1ms. This measurement is shown in figure 5.12 (b): when the frequency of the controlled AOM approaches the 200 MHz, the oscillation of the interference signal becomes slower. When the frequencies differ the most, also the interference signal oscillates fastest.

Finally, the PID unit of the RedPitaya was activated with the signal of PD 1 as input, to stabilise the phase of the two beams. This yielded the flat curves shown in figure 5.12 (c), showing that the phase between the beams can indeed be stabilized by controlling the AOMs. The values used for the stabilisation were  $p = 15$ ,  $i = 2000$ . The value to stabilize on was 0.1 in the units used in figure 5.12. The behaviour of the curve did not change significantly for longer recording times, up to 1s.

The interference contrast, defined by:

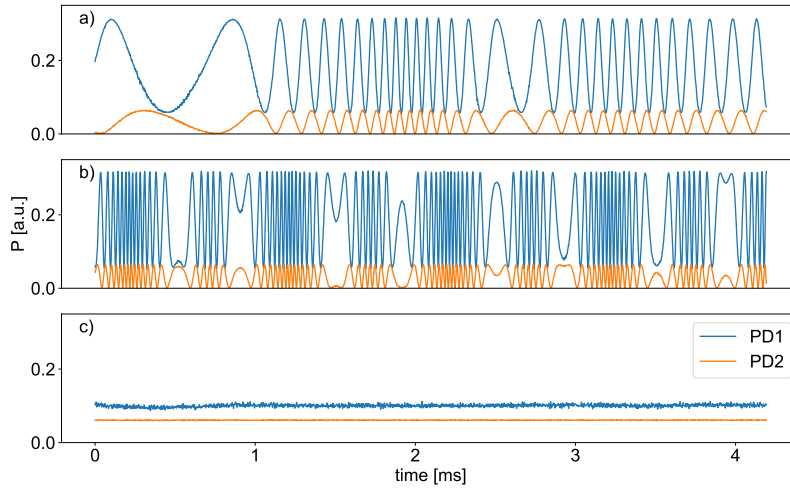


Figure 5.12.: Signal on both PDs, with both AOMs running constant (a), the controlled AOM varying its frequency by  $\pm 38\text{kHz}$  around 200 MHz in a triangle shape with a 1ms period (b) and with the PID unit acting on the signal on PD 1 (c).

$$C = 1 - \frac{P_{min}}{P_{max}}, \quad (5.9)$$

with the power at the maxima,  $P_{max}$  and minima  $P_{min}$  is 83 % for PD 1 and 94 % for PD 2.

### Analysis of the Signal on PD 2

The signal on PD 2 was actually expected to be constant, even when the AOMs are driven at different frequencies, as the optical path is always the same for both beams, and there should also be no frequency difference, as both beams pass through both AOMs. The measured signal can be explained by a mistake in the setup.

Both AOMs could have been aligned such, that only for the beams leaving the coupler, the first order was used, but for the beam pointing towards the coupler, the  $0^{th}$  order was used, resulting in no frequency shift by the second AOM for both beams. Therefore, the different frequencies visible at PD 1, would also occur on PD 2.

As shown in figure 5.13, it still would have been possible to achieve efficient fibre coupling, if the mistake was done in both AOMs.

In this case, the beams would not be overlapped between the AOMs. This could also explain the much lower achievable interference contrast on PD 1.

Unfortunately, the alignment procedure was not documented sufficiently precise, to

## 5. Experimental tests

allow the identification of such a mistake, but this is currently the only model, that can explain the data.

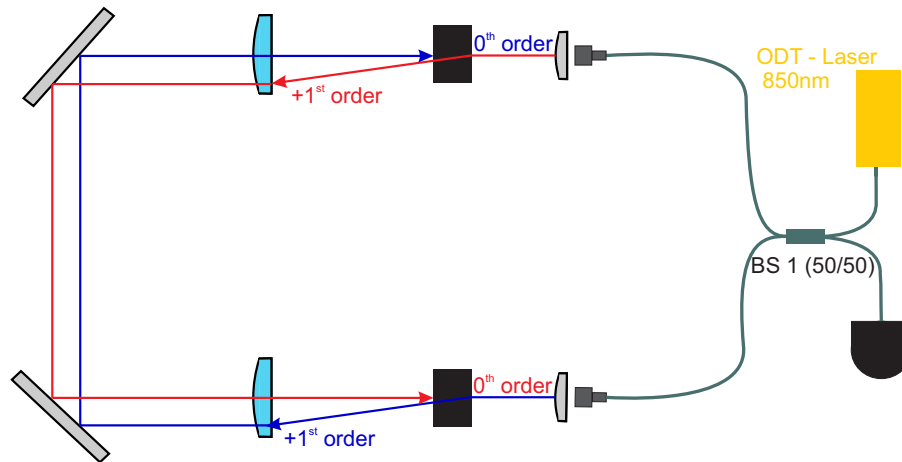


Figure 5.13.: Illustration of the suggested error in the setup. Lenses on the other sides of the AOMs, BS 2 and PD 1 are not shown for reasons of simplicity.

### 5.2.4. Summary

Even though it could not be finally identified, whether the suspected mistake in the alignment happened, it was shown, that an AOM, controlled by the RedPitaya PID can stabilize the phase of two laser beams, propagating in free space.

As mentioned above, the applicability of this method is limited, due to the required precise control of the AOM driving frequency. Additionally as visible in figure 5.12 (a), the usage of standard AOM drivers, introduces additional noise into the system, the stabilisation has to compensate for. Therefore, driving both AOMs from one source, where one channel can be tuned would be preferable. This was however not implemented.

For these reasons, in the final setup, the phase will be stabilised by a fibre-stretcher and an attenuator will be used to control the power of the second beam. An additional test setup to try these methods is planned.

## 6. Summary and Outlook

In this work the possibility to eliminate the decoherence effect of an atomic qubit, encoded in the  $m_F = \pm 1$  levels of the ground state of a  $^{87}\text{Rb}$ -atom, due to effective magnetic fields in a strongly focussed ODT with a standing wave trap is investigated.

In a linear polarized, tightly focussed ODT polarization effects create light fields, which affect the different  $m_F$  states of the ground level of the trapped atom in the same way as a magnetic field. This, together with residual fluctuations of the ambient magnetic field results in quick decoherence of a prepared state (see section 3.1).

The effect of magnetic fields in x- and y-direction up to 25 mG, on the atomic state can be eliminated by using a guiding field in z-direction. The effect of magnetic fluctuations in z-direction can be reduced strongly by transferring the atomic qubit to another basis, that is less sensitive to magnetic fields in z-direction. Thus, reducing the differences in the optically induced effective magnetic field below 25 mG will enable complete cancellation of this decoherence effect. This can be achieved by lowering the dipole trap depth, and applying longer cooling periods on the atom. These approaches were described in section 3.4.

But as this solution will result in a reduced repetition rate of the state preparation, it is preferable to cancel the effective fields entirely by using a standing wave trap configuration. If the ODT consists of two perfectly overlapped beams, the effective fields will cancel entirely. For non-perfect overlap, residual fields will remain. Their dependency on different misalignment parameters was described in section 4.3 and requirements on the alignment precision were derived.

In the standing wave potential, it is preferable to trap the atom in the central pockets to reduce differences in the residual effective magnetic field. It was found that this case can be identified by the fluorescence collected from the atom, and that on average 2.38 tries will be required to trap the atom in one of the central five pockets (see section 4.4).

Based on these theoretical considerations, a setup was built to test whether the alignment criteria found in chapter 4 could be met by using coupling to single mode fibres. With the non ideal setup, including objectives of different focal length and a telescope to compensate for that, the measured alignment parameters met the derived requirements up to maximally a factor of two, promising coherence times above 1 ms. Furthermore the influence of thermal fluctuations on the fibre coupling efficiency and the beam overlap was analysed, yielding that in the temperature stabilized environment of the experiment, active stabilisation will probably not be required. This test setup was described in section 5.1.

Additionally to the spatial overlap, active stabilisation of the relative phase of the beams will be required. One realisation of the phase stabilisation employing AOMs was built and tested as described in section 5.2. It was shown, that AOMs can be used for

## 6. Summary and Outlook

the phase stabilisation, but if driven from different sources, will introduce additional phase noise. Therefore, a fibre stretcher in combination with an attenuator will be tested in further experiments. A fibre stretcher will introduce only limited phase noise, however the attenuator will respond much slower than the AOMs. Yet, since increasing the intensities of the trap beams has to be done adiabatically anyway, the speed of the AOMs is not required.

Altogether the cancellation of the decoherence effect in a standing wave dipole trap, was shown in simulations and the realizability of this method with available tools was demonstrated. Hence, coherence times longer than 1 ms seem to be within reach in the near future.

# A. Coordinate System and Polarizations

This chapter will introduce the coordinate system used in this work, and define the photonic polarizations. These conventions are taken from [31]. The coordinate system is sketched in Figure A.1. Its origin is at the ideal position of the atom, hence the focus of the ODT. The axes are defined as follows:

- z-axis : along the optical axis of the objective pointing from the focus to the objective
- x-axis : perpendicular to the z-axis, parallel to the experimental table surface. Pointing towards the front wall of the glass cell.
- y-axis: perpendicular to the two other axis, pointing upwards

If cylindrical coordinates are used,  $\phi$  is measured from the positive x- towards the positive y-axis, the z-axis remains unchanged:

$$\begin{aligned} x &= r \cdot \cos(\phi) \\ y &= r \cdot \sin(\phi) \end{aligned} \tag{A.1}$$

Different polarizations of the readout beam or the photon emitted by the atom, are defined in Figure A.2 b). For the definition of the left- and right handedness, the historical convention, with view towards the source is applied. Note that the z-axis also has to be the quantization axis, to ensure the relations between the polarizations and

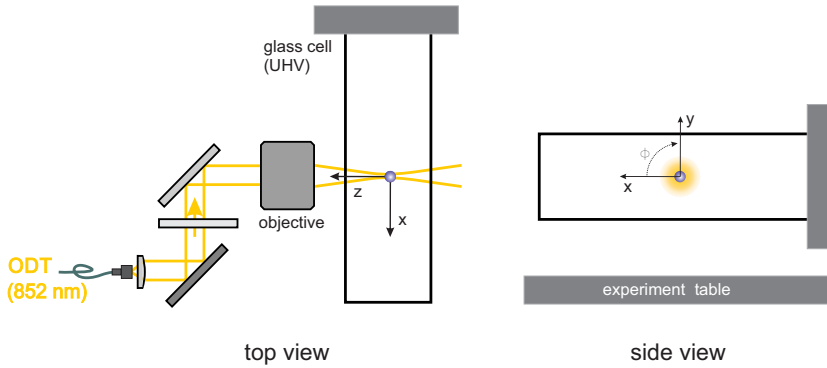


Figure A.1.: Coordinate System used in this work from two different views.

## A. Coordinate System and Polarizations

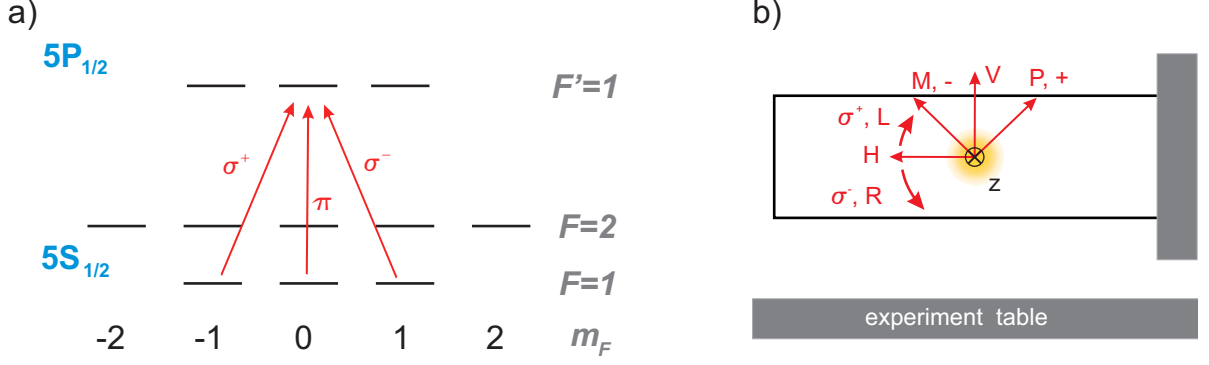


Figure A.2.: a) Effect of linear and circular polarization on the atomic states.  
b) Definition of different polarizations relative to the setup.

readout state	qubit state	atomic state	emitted pol.	$\chi_{ro}$
$ \Psi_H\rangle$	$ \uparrow\rangle_x$	$\frac{i}{\sqrt{2}}( 1, -1\rangle -  1, 1\rangle)$	H	H
$ \Psi_V\rangle$	$ \downarrow\rangle_x$	$\frac{1}{\sqrt{2}}( 1, -1\rangle +  1, 1\rangle)$	V	V
$ \Psi_P\rangle$	$ \uparrow\rangle_y$	$\frac{1}{\sqrt{2}}e^{i\frac{\pi}{4}}( 1, -1\rangle - i 1, 1\rangle)$	-	+
$ \Psi_M\rangle$	$ \downarrow\rangle_y$	$-\frac{1}{\sqrt{2}}e^{-i\frac{\pi}{4}}( 1, -1\rangle + i 1, 1\rangle)$	+	-
$ \Psi_L\rangle$	$ \uparrow\rangle_z$	$ 1, 1\rangle$	$\sigma^-$	$\sigma^+$
$ \Psi_R\rangle$	$ \downarrow\rangle_z$	$ 1, -1\rangle$	$\sigma^+$	$\sigma^-$

Table A.1.: List of atomic states, labeled by readout polarization, for which they are a dark state, qubit states, decomposition in  $m_F$  states, pol. of the emitted photon and readout pol  $\chi_{ro}$ .

atomic states, sketched in Figure A.2 a). Table A.1 summarizes the relations between polarizations, and certain atomic states.

## B. Quantification of the Circularity of Light

The AC-Stark shift of different atomic  $m_F$  states in an ODT, highly depends on the circularity of the ODT light [22]. In equation 2.1 the circularity is quantified by the parameter P. This chapter will explain the definition of this parameter.

The electric field vector of a laser beam in one plane orthogonal to the propagation direction can be written as [41]:

$$\vec{E} = \begin{pmatrix} E_x \cos(\omega t) \\ E_y \cos(\omega t + \Delta\varphi) \\ 0 \end{pmatrix} \quad (\text{B.1})$$

Where the z-axis is along the propagation direction, x and y are in the transversal plane.  $\omega = \frac{2\pi c}{\lambda}$  is the frequency of the laser and  $\lambda$  its wavelength. The Intensity of the laser beam at this position is  $I = \frac{1}{2}c\epsilon_0(E_x^2 + E_y^2)$ , with the components of the electric field in x and y direction  $E_x, E_y$ . In general the tip of this electric field vector will rotate in an ellipse. Orientation and ellipticity  $\epsilon$  of this ellipse can be tuned by varying the parameters  $E_x, E_y$  and  $\Delta\varphi$ . Observing the influence of  $\Delta\varphi$ , one can already see here, that maximum circularity will be reached for  $\Delta\varphi = \frac{\pi}{2}$  and with  $\Delta\varphi = 0/\pi$  the polarization will be linear, for any combination of  $E_x$  and  $E_y$ . P is now defined by:

$$P = \text{sign}(\Delta\varphi)\sqrt{1 - \epsilon^2} = \text{sign}(\Delta\varphi)\sqrt{1 - \left(\frac{|A|^2 - |B|^2}{|A|^2 + |B|^2}\right)^2} = \text{sign}(\Delta\varphi)\frac{2|A||B|}{|A|^2 + |B|^2} \quad (\text{B.2})$$

with A and B being the major and minor half axis of the ellipse.  $\epsilon$  can easily be measured, by placing a rotatable polariser in the beam and recording the highest and lowest transmitted Power ( $P_h, P_l$ ). Then  $\epsilon = \frac{P_h - P_l}{P_h + P_l}$  [22]. The situation is illustrated in Figure B.1

### Calculating the Semi Axes

A and B are the extrema of the length of  $\vec{E}$  over t. To simplify expressions,  $\omega t$  will be used as one variable here and the values, that extremize  $\vec{E}$  are called  $\omega t_{extr}$ . Like this,

## B. Quantification of the Circularity of Light

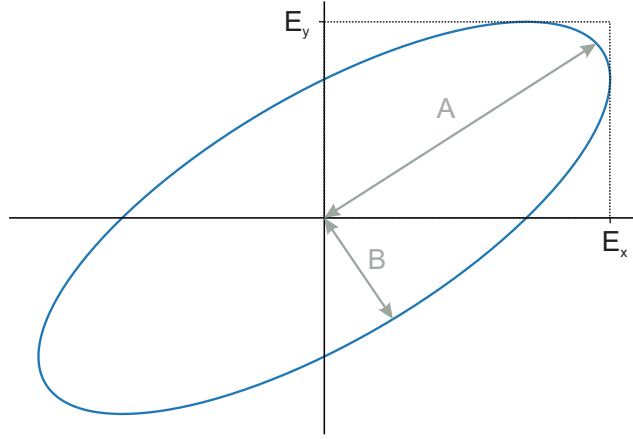


Figure B.1.: Polarisation ellipse for  $E_x = E_y$  and  $\Delta\varphi = \frac{\pi}{4}$

calculating A and B is straightforward by derivating the expression:

$$|\vec{E}| = \sqrt{(E_x \cos(\omega t))^2 + (E_y \cos(\omega t + \Delta\varphi))^2} \quad (\text{B.3})$$

The squareroot can be neglected for the derivative due to its strictly monotonic behavior.

$$\frac{d|\vec{E}|^2}{d\omega t} = -2E_x^2 \cos(\omega t)\sin(\omega t) - 2E_y^2 \cos(\omega t + \Delta\varphi)\sin(\omega t + \Delta\varphi) \quad (\text{B.4})$$

Using the identities:

$$\begin{aligned} \sin(a)\cos(a) &= \frac{1}{2}\sin(2a) \\ \sin(a+b) &= \cos(a)\sin(b) + \sin(a)\cos(b) \end{aligned} \quad (\text{B.5})$$

this simplifies to

$$\frac{d|\vec{E}|^2}{d\omega t} = -\sin(2\omega t)(E_x^2 + E_y^2\cos(2\Delta\varphi)) - \cos(2\omega t)E_y^2\sin(2\Delta\varphi) \quad (\text{B.6})$$

such, that the condition  $\frac{d|\vec{E}|^2}{d\omega t} := 0$  yields:

$$\omega t_{extr} = \frac{1}{2} \arctan \left( -\frac{E_y^2 \sin(2\Delta\varphi)}{E_x^2 + E_y^2 \cos(2\Delta\varphi)} \right) \quad (\text{B.7})$$

As  $\vec{E}$  is running on an ellipse, minima and maxima of its length, should alternate with a periodicity of  $\frac{\pi}{2}$ , therefore one can use the values at  $\omega t = \omega t_{extr}$  and  $\omega t = \omega t_{extr} + \frac{\pi}{2}$  for A and B in equation B.2.



## C. List of Abbreviations

Abbreviation	long term
ODT	Optical dipole trap
MOT	Magneto-optical trap
APD	Avalanche Photodiode
BSM	Bell-State-Measurement
UHV	ultra high vacuum
QFC	quantum frequency conversion
MBD	Maxwell-Boltzmann distribution
RW	running wave
SW	standing wave
AOM	acousto-optic modulator
PID	proportional integral derivative
FPGA	field programmable gate array



# D. Tables

## D.1. Physical Constants

Abbreviation	name	value
$c$	speed of light in vacuum	$2.99792458 \cdot 10^8 \frac{m}{s}$
$\hbar = \frac{h}{2\pi}$	reduced plancks constant	$1.054571726 \cdot 10^{-34} \text{ Js}$
$k_B$	Boltzmann constant	$1.38066 \cdot 10^{-23} \frac{J}{K}$
$\epsilon_0$	vacuum permittivity	$8.8541878128 \cdot 10^{-12} \frac{As}{Vm}$
$\mu_B$	Bohr magneton	$9.274009994 \cdot 10^{-24} \frac{J}{T}$

## D.2. Physical Properties of $^{87}\text{Rb}$

Abbreviation	name	value
$m$	mass	$87 \cdot 1.66 \cdot 10^{-27} kg$
$I$	nuclear spin	$\frac{3}{2}$

### D.3. Fit Parameters from the Knife Edge Measurements

$\eta$	$z_{0B}$ [ $\mu\text{m}$ ]	$w_{0B}$ [ $\mu\text{m}$ ]	$M_B$	$z_{0R}$ [ $\mu\text{m}$ ]	$w_{0R}$ [ $\mu\text{m}$ ]	$M_R$	$m_B$	$t_B$ [ $\mu\text{m}$ ]	$m_R$	$t_{0R}$ [ $\mu\text{m}$ ]
0.59	-4.1	2.6	1.00	-7.0	4.7	1.66	-0.0105	-31.5	-0.0057	-31.1
0.5	-4.0	2.6	0.99	-5.7	5.0	1.74	-0.0089	-31.2	-0.0043	-29.9
0.49	-2.8	2.5	0.98	-8.1	4.6	1.62	-0.0103	-32.4	-0.0061	-31.4
0.42	-3.4	2.4	0.95	-6.8	4.9	1.72	-0.0094	-31.9	-0.0045	-30.4
0.36	-2.7	2.7	1.02	-6.8	4.8	1.70	-0.0084	-31.3	-0.0041	-29.4
0.33	-2.1	2.7	1.01	-6.0	4.6	1.65	-0.0088	-30.3	-0.0042	-28.4
0.31	-3.7	2.6	0.98	-6.5	4.7	1.66	-0.0101	-30.1	-0.0058	-28.1
0.24	-4.9	2.6	0.97	-6.0	4.5	1.62	-0.0090	-30.7	-0.0047	-28.3
0.2	-5.7	2.6	1.01	-5.9	4.7	1.69	-0.0101	-30.7	-0.0061	-28.1
0.15	-4.6	2.7	1.02	-5.8	4.5	1.63	-0.0094	-31.3	-0.0052	-28.3
0.09	-4.4	2.7	1.04	-4.0	4.8	1.72	-0.0093	-31.4	-0.0057	-27.8
0.05	-4.0	2.7	1.01	-2.8	4.8	1.71	-0.0096	-31.4	-0.0065	-27.2

Table D.1.: Fit Parameters derived from the x-scans for the B(lue) and R(ed) beam

$\eta$	$z_{0B}$ [ $\mu\text{m}$ ]	$w_{0B}$ [ $\mu\text{m}$ ]	$M_B$	$z_{0R}$ [ $\mu\text{m}$ ]	$w_{0R}$ [ $\mu\text{m}$ ]	$M_R$	$m_B$	$t_B$ [ $\mu\text{m}$ ]	$m_R$	$t_{0R}$ [ $\mu\text{m}$ ]
0.58	-22.9	2.6	1.07	-11.1	5.3	1.85	0.0211	-31.8	0.0287	-31.8
0.49	-23.9	2.4	0.99	-8.9	5.2	1.80	0.0203	-31.2	0.0277	-30.6
0.49	-23.6	2.6	1.10	-14.5	5.4	1.92	0.0202	-33.4	0.0270	-32.8
0.41	-22.8	2.6	1.07	-13.6	5.4	1.88	0.0214	-32.7	0.0285	-31.9
0.34	-23.5	2.6	1.08	-12.6	5.3	1.85	0.0223	-32.1	0.0281	-31.1
0.33	-24.0	2.5	1.04	-12.0	5.3	1.84	0.0213	-31.5	0.0272	-30.4
0.31	-24.9	2.6	1.09	-15.6	5.4	1.87	0.0204	-31.7	0.0269	-31.4
0.24	-25.3	2.5	1.05	-15.2	5.4	1.90	0.0205	-31.4	0.0274	-31.3
0.23	-24.4	2.6	1.10	-15.7	5.5	1.91	0.0206	-31.9	0.0271	-32.0
0.15	-24.0	2.5	1.06	-15.4	5.4	1.89	0.0207	-31.6	0.0278	-31.7
0.08	-23.9	2.5	1.05	-14.0	5.4	1.90	0.0205	-31.7	0.0276	-31.7
0.05	-23.5	2.4	1.01	-12.6	5.3	1.88	0.0197	-31.5	0.0270	-31.7

Table D.2.: Fit Parameters derived from the y-scans for the B(lue) and R(ed) beam

# Bibliography

- [1] A. Agnesi and V. Degiorgio. Beam splitter phase shifts: Wave optics approach. *Optics and Laser Technology*, 95:72 – 73, 2017.
- [2] W. Alt. An objective lens for efficient fluorescence detection of single atoms. *Optik*, 113:142, 2002.
- [3] E. Wolf B. Richards and Dennis Gabor. Electromagnetic diffraction in optical systems, ii. structure of the image field in an aplanatic system. *Proc. R. Soc. Lond.*, (A253):358–379, 1997.
- [4] M.C.Teich B.E.A. Saleh. *Fundamentals of Photonics*. John Wiley and Sons, Inc., 1991.
- [5] J. S. Bell. On the einstein podolsky rosen paradox. *Physics Physique Fizika*, 1:195–200, Nov 1964.
- [6] Charles Bennett. Quantum information and computation. *Physics Today*, 1995.
- [7] A. Boivin and E. Wolf. Electromagnetic field in the neighborhood of the focus of a coherent beam. *Phys. Rev.*, 138:B1561–B1565, Jun 1965.
- [8] H.-J. Briegel, W. Dür, J. I. Cirac, and P. Zoller. Quantum repeaters: The role of imperfect local operations in quantum communication. *Phys. Rev. Lett.*, 81:5932–5935, Dec 1998.
- [9] Daniel Burchardt. *A Rigorous Test of Bell’s Inequality and Quantum Teleportation Employing Single Atoms*. PhD thesis, 2017.
- [10] John F. Clauser, Michael A. Horne, Abner Shimony, and Richard A. Holt. Proposed experiment to test local hidden-variable theories. *Phys. Rev. Lett.*, 23:880–884, Oct 1969.
- [11] Claude Cohen-Tannoudji and Jacques Dupont-Roc. Experimental study of zeeman light shifts in weak magnetic fields. *Phys. Rev. A*, 5:968–984, Feb 1972.
- [12] J. Dalibard and C. Cohen-Tannoudji. Laser cooling below the doppler limit by polarization gradients: simple theoretical models. *J. Opt. Soc. Am. B*, 6(11):2023–2045, November 1989.
- [13] A. Einstein, B. Podolsky, and N. Rosen. Can quantum-mechanical description of physical reality be considered complete? *Phys. Rev.*, 47:777–780, May 1935.

## Bibliography

- [14] C.J. Foot. *Atomic Physics*. Oxford University Press, 2005.
- [15] Marissa Giustina, Marijn A. M. Versteegh, Sören Wengerowsky, Johannes Handsteiner, Armin Hochrainer, Kevin Phelan, Fabian Steinlechner, Johannes Kofler, Jan-Åke Larsson, Carlos Abellán, Waldimar Amaya, Valerio Pruneri, Morgan W. Mitchell, Jörn Beyer, Thomas Gerrits, Adriana E. Lita, Lynden K. Shalm, Sae Woo Nam, Thomas Scheidl, Rupert Ursin, Bernhard Wittmann, and Anton Zeilinger. Significant-loophole-free test of bell’s theorem with entangled photons. *Phys. Rev. Lett.*, 115:250401, Dec 2015.
- [16] Rudolf Grimm and Matthias Weidemüller. Optical dipole traps for neutral atoms. *arXiv:physics/9902072v1*, 1999.
- [17] Florian Henkel. *Photoionisation detection of single Rb-87 atoms using channel electron multipliers*. PhD thesis, 2011.
- [18] Bernien H. Dréau A. et al. Hensen, B. Loophole-free bell inequality violation using electron spins separated by 1.3 kilometres. *Nature*, 526:682–686, 2015.
- [19] Julian Hofmann. *Heralded Atom-Atom Entanglement*. PhD thesis, LMU, 2013.
- [20] M. Żukowski, A. Zeilinger, M. A. Horne, and A. K. Ekert. “event-ready-detectors” bell experiment via entanglement swapping. *Phys. Rev. Lett.*, 71:4287–4290, Dec 1993.
- [21] H. J. Kimble. The quantum internet. *Nature*, 453(7198):1023–1030, Jun 2008.
- [22] K.L.Corwin, M.Kuppens S.J, D.Cho, and C.E.Wieman. Spin-polarized atoms in a circularly polarized optical dipole trap. *Physical Review Letters*, 83(7):1311–1314, August 1999.
- [23] Paul Koschmieder. Efficient control of magnetic fields in single atom experiments. Master’s thesis, LMU, 2019.
- [24] Claude Cohen-Tannoudji; Bernard Diu; Franck Laloe. *Quantum Mechanics*. 1977.
- [25] Chien-Ju Lee. Observing single atoms. Master’s thesis, LMU, 2011.
- [26] N. Lütkenhaus, J. Calsamiglia, and K.-A. Suominen. Bell measurements for teleportation. *Phys. Rev. A*, 59:3295–3300, May 1999.
- [27] S.Langefeld A.Neunzer S.Ritter G.Rempe M.Körber, O.Morin. Decoherence-protected memory for a single-photon qubit. *Nature photonics*, 12:18–21, January 2018.
- [28] Leonhard Neuhaus. *pyrpl Documentation*, 0.9.4.0 edition, 2017.
- [29] Norbert Ortegel. *State readout of single Rubidium-87 atoms for a loophole-free test of Bell’s inequality*. PhD thesis, 2016.

- [30] Jian-Wei Pan, Dik Bouwmeester, Harald Weinfurter, and Anton Zeilinger. Experimental entanglement swapping: Entangling photons that never interacted. *Phys. Rev. Lett.*, 80:3891–3894, May 1998.
- [31] Kai Stefan Matthias Redeker. *Entanglement of single Rubidium Atoms: From a Bell Test Towards Applications*. PhD thesis, 2020.
- [32] Wenjamin Rosenfeld. *Experiments with an Entangled System of a Single Atom and a Single Photon*. PhD thesis, LMU, 2008.
- [33] Wenjamin Rosenfeld, Daniel Burchardt, Robert Garthoff, Kai Redeker, Norbert Ortengel, Markus Rau, and Harald Weinfurter. Event-ready bell test using entangled atoms simultaneously closing detection and locality loopholes. *Phys. Rev. Lett.*, 119:010402, Jul 2017.
- [34] N. Schlosser, G. Reymond, and P. Grangier. Collisional blockade in microscopic optical dipole traps. *Phys. Rev. Lett.*, 89:023005, Jun 2002.
- [35] Matthias Seubert. Title: to be announced. Master’s thesis, LMU, 2020.
- [36] Daniel A. Steck. Rubidium 87 d line data. Technical report, N 2019.
- [37] Ernest Y.-Z. Tan, Charles C.-W. Lim, and Renato Renner. Advantage distillation for device-independent quantum key distribution. *Phys. Rev. Lett.*, 124:020502, Jan 2020.
- [38] Tim van Leent, Matthias Bock, Robert Garthoff, Kai Redeker, Wei Zhang, Tobias Bauer, Wenjamin Rosenfeld, Christoph Becher, and Harald Weinfurter. Long-distance distribution of atom-photon entanglement at telecom wavelength. *Phys. Rev. Lett.*, 124:010510, Jan 2020.
- [39] Jürgen Volz, Markus Weber, Daniel Schlenk, Wenjamin Rosenfeld, Johannes Vrana, Karen Saucke, Christian Kurtsiefer, and Harald Weinfurter. Observation of entanglement of a single photon with a trapped atom. *Phys. Rev. Lett.*, 96:030404, Jan 2006.
- [40] Markus Weber. *Quantum optical experiments towards atom-photon entanglement*. PhD thesis, LMU, 2005.
- [41] Ursula Zinth Wolfgang Zinth. *Optik*. 4 edition, 2013.



# Danksagung

Zuletzt, möchte ich allen danken die zum entstehen dieser Masterarbeit beigetragen haben:

- Prof. Harald Weinfurter, für die Chance diese Arbeit in seiner Gruppe anzufertigen und die offene Arbeitsatmosphäre.
- allen Mitgliedern des Atom Projekts, für viele hilfreiche Diskussionen und Geduld bei Fragen aller Art. Insbesondere Tim van Leent und Kai Redeker für die Einführung in das Laborhandwerk.
- allen Mitgliedern der AG-Weinfurter für die freundliche Aufnahme und die schöne Zeit. Vor allem Martin Zeitlmair für viele Ratschläge mit Softwareproblemen und die Hilfe beim Schmieden von Morgulklingen.
- all meinen Freunden dafür, dass sie eine immer willkommene Ablenkung sind. Im besonderen Clément, für viele unvergessliche Momente in den Bergen der Welt.
- Julia dafür, dass sie immer für mich da ist.
- meinen Eltern Yalçin und Annette dafür, dass sie alles unterstützen, was ich tue.



# Erklaerung

Mit der Abgabe dieser Masterarbeit versichere ich, dass ich die Arbeit selbststaendig verfasst und keine anderen als die angegebenen Quellen und Hilfsmittel verwendet habe.

München, den 13. Mai 2020

Derya Taray